Naval Research Laboratory
Washington, DC 20375-5320

NRL/MR/6790--97-7948

Propagation and Stability of Intense Laser Pulses in Partially-Stripped Plasmas

P. SPRANGLE
E. ESAREY

Beam Physics Branch
Plasma Physics Division

B. HAFIZI

ICARUS Research, Inc.
P.O. Box 30780
Bethesda, MD

July 21, 1997

REPORT DOCUMENTATION PAGE

Form Approved
OMB No. 0704-0188

1. AGENCY USE ONLY (*Leave Blank*)	2. REPORT DATE	3. REPORT TYPE AND DATES COVERED
	July 21, 1997	Interim

4. TITLE AND SUBTITLE

Propagation and Stability of Intense Laser Pulses in Partially-Stripped Plasmas

5. FUNDING NUMBERS

6. AUTHOR(S)

P. Sprangle, E. Esarey, and B. Hafizi*

7. PERFORMING ORGANIZATION NAME(S) AND ADDRESS(ES)

Naval Research Laboratory
Washington, DC 20375-5320

8. PERFORMING ORGANIZATION REPORT NUMBER

NRL/MR/6790--97-7948

9. SPONSORING/MONITORING AGENCY NAME(S) AND ADDRESS(ES)

Office of Naval Research
800 North Quincy Street
Arlington, VA 22217-5660

Department of Energy
Washington, DC 20585

10. SPONSORING/MONITORING AGENCY REPORT NUMBER

11. SUPPLEMENTARY NOTES

*ICARUS Research, Inc.
P.O. Box 30780
Bethesda, MD 20824-0780

12a. DISTRIBUTION/AVAILABILITY STATEMENT

Approved for public release; distribution unlimited.

12b. DISTRIBUTION CODE

13. ABSTRACT (*Maximum 200 words*)

The propagation and stability of intense laser pulses in a partially-stripped plasma, i.e., in the presence of free and bound electrons, is analyzed. The presence of bound electrons is shown to significantly alter the propagation and stability of intense laser pulses. The bound electrons are represented by a linear and nonlinear susceptibility, while the free electrons, which can support plasma waves, are treated nonlinearly. In the presence of both free and bound electrons, an atomic modulation instability develops that can have a growth rate substantially higher than either the conventional relativistic modulational instability or the forward Raman instability. Bound electrons can also greatly enhance the filamentation instability. The backward Raman instability, however, is unaffected by bound electrons.

14. SUBJECT TERMS

Partially-stripped plasama
Nonlinear susceptibility
Modulation instability
Raman instability
Self-phase modulation
Group velocity dispersion

15. NUMBER OF PAGES

62

16. PRICE CODE

17. SECURITY CLASSIFICATION OF REPORT	18. SECURITY CLASSIFICATION OF THIS PAGE	19. SECURITY CLASSIFICATION OF ABSTRACT	20. LIMITATION OF ABSTRACT
UNCLASSIFIED	UNCLASSIFIED	UNCLASSIFIED	UL

NSN 7540-01-280-5500

Standard Form 298 (Rev. 2-89)
Prescribed by ANSI Std 239-18
298-102

Contents

PROPAGATION AND STABILITY OF INTENSE LASER PULSES IN PARTIALLY-STRIPPED PLASMAS

I. Introduction

The propagation of intense laser pulses in plasmas is relevant to a wide range of applications, such as x-ray lasers [1-5], laser fusion [6-8], laser-plasma accelerators [9-18], harmonic generation in plasmas and gases [19-23], and laser-plasma channeling [24-30]. In many intense laser-plasma experiments the ions are not fully stripped and hence the propagation medium consists of both free and bound electrons. We find that bound electrons can lead to an atomic modulation instability (AMI) which can dominate the conventional relativistic modulational instability (RMI) [31-33] and forward Raman scattering (FRS) instability [34-38]. The AMI requires both free and bound electrons, i.e., the free electrons provide anomalous group velocity dispersion whereas the bound electrons provide self-phase modulation. Bound electrons can also result in an atomic filamentation instability (AFI), which can dominate the conventional relativistic filamentation instability (RFI) [31-33]. These effects could play an important role in laser interaction experiments with high-Z material.

Generally speaking, the refractive index associated with an intense laser pulse in a partially-stripped plasma is $\eta = 1 + \Delta\eta$, with $\Delta\eta = \eta_0 - 1 + \Delta\eta_\perp + \Delta\eta_p + \Delta\eta_{pw} + \Delta\eta_r + \Delta\eta_a$, where $\eta_0 \cong 1$ is the linear index associated with the bound (atomic) electrons, $\Delta\eta_\perp = -2c^2/(\omega_0 r_0)^2$ is the contribution from the finite spot size of the laser pulse, $\Delta\eta_p = -\omega_p^2 / 2\omega_0^2$ is the linear contribution from the free (plasma) electrons, $\Delta\eta_{pw} = \Delta\eta_p(\delta n_p/n_p)$, is the nonlinear contribution from the excited plasma wave, $\Delta\eta_r = -\Delta\eta_p a_0^2 / 4$ is the relativistic contribution from plasma electrons and $\Delta\eta_a = \eta_2 I$ is the nonlinear contribution from the bound atomic electrons. In the above, ω_0 is the laser frequency , r_0 is the laser spot size, $\omega_p = (4\pi q^2 n_p/m)^{1/2}$ is the plasma frequency, n_p is the ambient plasma density, δn_p is the perturbed plasma density, a_0 the

Manuscript approved May 12, 1997.

normalized (unitless) peak amplitude of the laser vector potential, η_2 is the nonlinear refractive index associated with the bound electrons, I is the time averaged laser intensity, and it is assumed that $|\Delta\eta| << 1$. For a linearly polarized laser beam $a_0^2 = 7.32 \times 10^{-19} \lambda_0^2 [\mu m] I[W/cm^2]$, where $\lambda_0 = 2\pi c/\omega_0$ is the laser wavelength. Note that a_0 is equal to the peak electron oscillation momentum in the laser pulse, normalized to mc.

Self-focusing of the laser beam requires that the radial gradient of the refractive index be negative, i.e., $\partial\Delta\eta / \partial r < 0$. It can be shown that the condition for self-focusing is $(\pi r_0/\lambda_0)^2 \Delta\eta_{r,a} \geq 1$, where $r_0^2 \Delta\eta_{r,a}$ is proportional to the laser power. This implies that the refractive indices associated with the relativistic plasma $\Delta\eta_r$ and bound electrons $\Delta\eta_a$ can individually cause focusing of the laser pulse if certain critical power levels are exceeded. The critical powers for relativistic focusing in a plasma [31,39-41] and nonlinear focusing in a gas [42-44] are, respectively,

$$P_p = 2c(q / r_e)^2 (\omega_0 / \omega_p)^2, \tag{1a}$$

and

$$P_a = \lambda_0^2 / (2\pi\eta_0\eta_2), \tag{1b}$$

where $r_e = q^2/mc^2 = 2.82 \times 10^{-13}$ cm is the classical electron radius. In practical units, the relativistic focusing power in Eq. (1a) can be written as $P_p [GW] = 17.4(\omega_0/\omega_p)^2$. The ratio of the critical powers can be much greater than unity and scales with laser frequency to the fourth power. In practical units,

$$R = \frac{P_p}{P_a} = \frac{1.22 \times 10^{40} \eta_0 \eta_2 [cm^2 / W]}{\lambda_0^4 [\mu m] n_p [cm^{-3}]}, \tag{2}$$

where η_2 is proportional to the atomic gas density, n_a. For example, taking $\eta_2 \cong 10^{-19}$ cm^2/W for typical neutral gases at standard temperature and pressure (STP), $n_a = n_p = 2.7 \times 10^{19}$ cm^{-3} and $\lambda_0 = 0.5$ μm, we find that $R \cong 710$. For these parameters, the critical powers for relativistic plasma and nonlinear gas focusing are $P_p = 2.8$ TW and $P_a = P_p/710 = 3.9$ GW, respectively. In a partially-stripped plasma, if $R >> 1$, the bound electrons have a much greater effect on the focusing of the laser pulse than the free electrons.

This paper is organized as follows. Section II discusses the wave equation for a laser pulse propagating in a partially-stripped plasma. The polarization field of the bound electrons and the plasma current are retained to third order in the laser field. The nonlinear dispersion relation for the pump laser field is discussed in Sec. III. The nonlinear dispersion relation for the Stokes and anti-Stokes sidebands is derived in Sec. IV. Growth rates are derived for (a) modulation, (b) Raman and (c) filamentation instabilities and are plotted as functions of wavenumber for several values of R. The physical mechanism of the AMI is also discussed and the roles of both the bound and free electrons is clearly delineated. A discussion and conclusion is given in Sec. V. This paper also includes two appendices discussing (A) the nonlinear susceptibility and group velocity dispersion parameter and (B) ionization rates due to both photo and collisional processes.

II. Nonlinear Wave Equation

The wave equation for a laser pulse propagating in a partially-stripped plasma is

$$\left(\nabla^2 - c^{-2}\partial^2 / \partial t^2\right)\underset{\sim}{E} = 4\pi c^{-2}\left(\partial^2 \underset{\sim}{P}/\partial t^2 + \partial \underset{\sim}{J}_p/\partial t\right), \qquad (3)$$

where $\underset{\sim}{E}$ is the laser electric field, $\underset{\sim}{P}$ is the polarization field associated with the bound electrons and $\underset{\sim}{J}_p$ is the plasma current density. The polarization field consists of a linear and nonlinear part, $\underset{\sim}{P} = \left(\chi^{(1)} + \chi^{(3)}(\underset{\sim}{E} \bullet \underset{\sim}{E})\right)\underset{\sim}{E}$, where $\chi^{(1)}$ ($\chi^{(3)}$) is the linear (third order) susceptibility associated with the bound electrons. The time averaged refractive index of the bound electrons is $\eta = \eta_0 + \eta_2 I$, where $\eta_0 = (1 + 4\pi\chi^{(1)})^{1/2}$ is the linear index, $\eta_2 = 8\pi^2\chi^{(3)}/\ \eta_0^2 c$ is the nonlinear refractive index and $I = (c/4\pi)\eta_0 < \underset{\sim}{E} \bullet \underset{\sim}{E} >$ is the time averaged laser intensity. In the present model, the origin of the third order susceptibility $\chi^{(3)}$ (or nonlinear index η_2) is the anharmonic potential well in which the bound electrons oscillate. The response time for the development of $\chi^{(3)}$ (or η_2) due to the anharmonic electron oscillations is fast, on the order of 10^{-15} sec.

Values of $\chi^{(3)}$ for partially-stripped atoms are not commonly known but can be readily calculated. For the purpose of estimating these values, we will assume the charge state is small compared to the atomic number, and therefore $\chi^{(3)}$ for a partially-stripped atom is expected to be within an order of magnitude of the neutral atom value. Near atomic resonances, however, significant changes in $\chi^{(3)}$ and $\chi^{(1)}$ can occur. It is important to note that the validity of the present analysis is not contingent on $\chi^{(3)}$ being accurately known. Our results are expressed in terms of the quantity R, which is the effective value for a partially-stripped atom and proportional to $\chi^{(3)}$, and examples are given for a wide range of R. Estimates for $\chi^{(3)}$ associated with neutral and charged atoms at frequencies far below resonance are given in Appendix A.

The assumption that the average charge state is small compared to the atomic number places limitations on the laser intensity and duration. Nonetheless, our model is expected to hold for a wide range of laser intensities and pulse durations. There are two limits on the laser

intensity: (i) the intensity must be lower than the threshold for ionization of the next charge state and (ii) the intensity must be sufficiently small so that the perturbation expansion of $\underset{\sim}{P}$ remains valid. In addition, the laser pulse length must be sufficiently short so as to avoid further electron collisional ionization. Appendix B discusses and estimates photo and collisional ionization rates as a function of laser intensity and ionization energies. Intensities and pulse durations needed to avoid ionization, beyond certain levels, are estimated in Appendix B.

For the expansion of the polarization field in powers of the field to be valid we require $\eta_2 I < \eta_0 - 1$, which in terms of a_0^2 is

$$a_0^2 << 7.32 \text{ x } 10^{-19}(\eta_0 - 1)\lambda_0^2[\mu m] / \eta_2[cm^2 / W], \tag{4}$$

where both $\eta_0 - 1$ and η_2 are proportional to the atomic gas density n_a. As an example, for N_2 at STP with $\lambda_0 = 1$ μm, $\eta_0 - 1 = 3 \text{ x } 10^{-4}$, $\eta_2 = 10^{-19}$ cm^2/W and the normalized laser amplitude is limited to $a_0 << 0.05$, which corresponds to an intensity $I << 3.5 \text{ x } 10^{15}$ W/cm^2. The quantity Ra_0^2 is an important parameter in determining the stability properties of the laser pulse, which in practical units is given by

$$Ra_0^2 = 8.93 \text{ x } 10^{21} \frac{\eta_2[cm^2 / W]I[W / cm^2]}{\lambda_0^2[\mu m]n_p[cm^{-3}]}, \tag{5}$$

where $\eta_2 I << \eta_0 - 1$ for the expansion to be valid.

The plasma current density, correct to third order in $\underset{\sim}{a}$, is [9,36,38]

$$\underset{\sim}{J}_p = qn_p c\left(1 + \delta n_p / n_p - \underset{\sim}{a} \bullet \underset{\sim}{a} / 2\right)\underset{\sim}{a}, \tag{6}$$

where the term proportional to $\underset{\sim}{a} \bullet \underset{\sim}{a}$ is due to relativistic changes in the electron mass. The perturbed plasma density [9,36,38] is given by

$$\left(\partial^2 / \partial t^2 + \omega_p^2\right)\delta n_p / n_p = (c^2 / 2)\nabla^2(\underset{\sim}{a}\bullet \underset{\sim}{a}). \qquad (7)$$

It is convenient to write the wave equation in Eq. (3) in terms of the normalized vector potential $\underset{\sim}{a}$, and to use the Coulomb gauge, $\nabla \bullet \underset{\sim}{a} = 0$. The radiation field is assumed to consist of plane waves polarized in the x-direction of the form $\underset{\sim}{a} = (a_p + a_+ + a_-)\hat{e}_x$ where a_p denotes the pump wave, $a_\pm$ are the anti-Stokes and Stokes sidebands, and $|a_\pm| << |a_p|$. The pump wave is represented by $a_p = (a_0/2)\exp(i(k_0 z - \omega_0 t)) + c.c.$, while the sidebands are given by

$a_+ = (\hat{a}_+ / 2)\exp\left[i\left((k_0 + k)z + k_\perp y - (\omega_0 + \omega)t\right)\right] + c.c.$, and

$a_- = (\hat{a}_- / 2)\exp\left[i\left((k_0 - k)z - k_\perp y - (\omega_0 - \omega^*)t\right)\right] + c.c.$, where k_0 and ω_0 are the wavenumber and frequency of the pump, k, $k_\perp$, and ω are the real axial wavenumber, real transverse wavenumber and complex frequency of the sidebands and * denotes the complex conjugate. The amplitude of the pump and sidebands are real and given by a_0 and $\hat{a}_\pm$, respectively, and $\nabla^2 = \partial^2/\partial y^2 + \partial^2/\partial z^2$. Substituting Eq. (6) together with the polarization field in terms of $\underset{\sim}{a}$, into Eq. (3) yields the following wave equation for $\underset{\sim}{a}$,

$$\left(\nabla^2 - \eta_0^2 c^{-2}\frac{\partial^2}{\partial t^2} - k_p^2\right)\underset{\sim}{a} = k_p^2\frac{\delta n_p}{n_p}\underset{\sim}{a}$$

$$-\frac{k_p^2}{2}\left[(\underset{\sim}{a}\bullet\underset{\sim}{a})\underset{\sim}{a} - R\omega_0^{-4}\frac{\partial}{\partial t}\left(\left(\frac{\partial \underset{\sim}{a}}{\partial t}\bullet\frac{\partial \underset{\sim}{a}}{\partial t}\right)\frac{\partial \underset{\sim}{a}}{\partial t}\right)\right], \qquad (8)$$

where $k_p = \omega_p/c$ and R is the effective value in a partially-stripped plasma. In deriving Eq. (8), $\chi^{(1)}$ and $\chi^{(3)}$ are assumed to be constants and independent of laser frequency. This assumption is valid since group velocity dispersion is dominated by the free electrons and not the bound

electrons, as discussed in Appendix A. The third order nonlinear source current, which is proportional to the right-hand side of Eq. (8), significantly alters the propagation and stability of the intense laser beam. Sidebands can be generated, resulting in various types of modulation, filamentation, and Raman instabilities.

III. Nonlinear Pump Dispersion and Propagation

The nonlinear dispersion relation for a linearly polarized pump wave is

$$\eta_0^2\omega_0^2 / c^2 - k_0^2 - k_p^2 + k_p^2\left(\alpha_0 a_0^2 + (3/8)Ra_0^2\right) = 0, \qquad (9)$$

where R is given by Eq. (2) and $\alpha_0 = 3/8 - (1/8)(ck_0)^2 / (\omega_0^2 - \omega_p^2/4)$ is due to relativistic and nonlinear plasma wave effects. The term proportional to $(3/8)Ra_0^2$ in Eq. (9) represents the nonlinear effects of the bound electrons and can be substantially greater than the plasma term $\alpha_0 a_0^2 \cong a_0^2/4$. The resonant term in the expression for α_0, i.e., the term proportional to $1/(\omega_0^2 - \omega_p^2/4)$, is due to the nonlinear plasma wave at frequency and wavenumber $(2\omega_0, 2k_0)$. The cut-off frequency is given by

$$\omega_c = (\omega_p / \eta_0)\left(1 - (3/16)(1+R)a_0^2\right), \qquad (10)$$

where $Ra_0^2 << 1$. Note that a lower branch of the dispersion relation at $\omega_0 = \omega_p/2$ exists. The model, however, is not valid when $\omega_0 \cong \omega_p/2$ since from Eq. (7), the perturbed density $\delta n_p/n_p$ can be large. For a circularly polarized pump wave $\underset{\sim}{a}^* \cdot \underset{\sim}{a} = a_0^2$ is a constant and the dispersion relation is

$$\eta_0^2\omega_0^2/c^2 - k_0^2 - k_p^2\left[1-(1+R)a_0^2/2\right]=0. \tag{11}$$

A circularly polarized pump wave does not induce a plasma wave and therefore the resonant term in the expression for α_0, is not present. For a circularly polarized pump the cut-off frequency is given by

$$\omega_c = (\omega_p/\eta_0)\left(1-(1+R)a_0^2/4\right). \tag{12}$$

In the present model propagation slightly below the plasma frequency is achieved as a result of the partial cancellation of the linear plasma current by the nonlinear polarization current due to the bound electrons. Propagation far below the plasma frequency, however, can result from a cancellation of the linear plasma current by a nonlinear plasma current induced from the beating of two electromagnetic fields. This is referred to as electromagnetically induced transparency in plasmas [45].

IV. Sideband Dispersion and Stability

To analyze the instabilities, Eqs. (7) and (8) are solved to order $a_0^2\hat{a}_\pm$ giving

$$D_+\hat{a}_+ = \Omega_0^2\left[c^2(k^2+k_\perp^2)/D - 1 - (3/2)R(2(\omega_0+\omega)^2-\omega_0^2)/\omega_0^2\right]\hat{a}_+$$

$$+\Omega_0^2\left[c^2(k^2+k_\perp^2)/D - 1 - (3/2)R(\omega_0^2-\omega^2)/\omega_0^2\right]\hat{a}_-^*, \tag{13a}$$

$$D_-\hat{a}_-^* = \Omega_0^2\left[c^2(k^2+k_\perp^2)/D - 1 - (3/2)R(2(\omega_0-\omega)^2-\omega_0^2)/\omega_0^2\right]\hat{a}_-^*$$

$$+\left[c^2(k^2+k_\perp^2)/D - 1 - (3/2)R(\omega_0^2-\omega^2)/\omega_0^2\right]\hat{a}_+, \tag{13b}$$

where $D_{\pm} = \eta_0^2\omega^2 - c^2(k^2 + k_\perp^2) \pm 2(\eta_0^2\omega_0\omega - c^2k_0k)$, $\Omega_0^2 = \omega_p^2 a_0^2 / 4$ and $D = \omega^2 - \omega_p^2$.

Combining Eqs. (13a) and (13b) we obtain the dispersion relation

$$\left[D_+ - \Omega_0^2\left\{c^2(k^2 + k_\perp^2)/D - 1 - (3/2)R\left(2(\omega_0 + \omega)^2 - \omega_0^2\right)/\omega_0^2\right\}\right]\bullet$$

$$\left[D_- - \Omega_0^2\left\{c^2(k^2 + k_\perp^2)/D - 1 - (3/2)R\left(2(\omega_0 - \omega)^2 - \omega_0^2\right)/\omega_0^2\right\}\right]$$

$$= \Omega_0^4\left(c^2(k^2 + k_\perp^2)/D - 1 - (3/2)R(\omega_0^2 - \omega^2)/\omega_0^2\right)^2. \qquad (14)$$

In the limit $R \to 0$, Eq. (14) reduces to previous results [33]. If the sideband frequency is near the carrier frequency, $|\omega| << \omega_0$, the dispersion relation reduces to

$$\left(\omega^2 - c^2(k^2 + k_\perp^2)\right)^2 - 4\omega_0^2(\omega - \beta_0 ck)^2$$

$$+ 2\Omega_0^2\left((3/2)R + 1 - c^2(k^2 + k_\perp^2)/(\omega^2 - \omega_p^2)\right)\left(\omega^2 - c^2(k^2 + k_\perp^2)\right) = 0, \quad (15)$$

where $\beta_0 = ck_0 / \omega_0$ and we have set $\eta_0 = 1$. The contribution from the bound electrons, i.e., the term proportional to R, can be significant and can dramatically modify the conventional RMI, RFI, and FRS instability.

a. Modulational Instability

The presence of bound electrons in a partially-stripped plasma can result in an AMI which can completely dominate both the conventional RMI and the FRS instability for $R >> 1$. Since the AMI and RMI are not driven by the induced plasma wave, they can be analyzed by neglecting the resonant plasma wave term, i.e., the term proportional to $c^2(k^2 + k_\perp^2)/(\omega^2 - \omega_p^2)$ in the dispersion relation of Eq. (15). Setting $\omega = \beta_0 ck + \delta\omega$ and $k_\perp = 0$ in Eq. (15), we find that for the AMI and RMI

$$\delta\omega = -(\omega_p/\omega_0)^2(ck/2)\Big[(ck/\omega)^2 - (3/8)a_0^2$$

$$\pm\Big(-(1+3R/2)a_0^2/2 + (ck/\omega_0)^2\Big)^{1/2}\Big], \qquad (16)$$

where $\beta_0 ck >> |\delta\omega|$. The AMI growth rate is

$$\Gamma = (1/2)(\omega_p/\omega_0)^2 ck\Big((1+3R/2)a_0^2/2 - (ck/\omega_0)^2\Big)^{1/2}, \qquad (17)$$

and extends from $k = 0$ to $k = k_{max} = (a_0\omega_0/\sqrt{2}c)(1+3R/2)^{1/2}$ and peaks at $k = k_{max}/\sqrt{2}$. In the conventional RMI the range of unstable wave numbers is restricted to $k < \omega_p/c$ while in the AMI the range in k can exceed ω_p/c and can approach ω_0/c. Since the range of wavenumbers over which the AMI exists is broad, it will be less sensitive to laser incoherence or plasma inhomogeneities than the RMI or FRS instability. The maximum growth rate for the AMI is given by

$$\Gamma = (\omega_p^2 a_0^2/8\omega_0)(1+3R/2). \qquad (18)$$

The maximum growth rate for the conventional RMI ($R = 0$) [31,33] is $\Gamma = (1/8)(\omega_p^2/\omega_0)a_0^2$ and occurs at $k = (a_0/2)\omega_0/c << k_{max}$. The ratio of the maximum growth rate for the AMI to the conventional RMI is $1 + 3R/2$, which can be much greater than unity. In the limit $n_p \to 0$, Eq. (17) implies that $k_{max} \to \infty$ and, for finite k, the AMI growth rate scales as $\Gamma \sim n_p^{1/2} \to 0$, hence, the AMI is stable in the absence of a plasma.

b. Raman Instability

The growth rate for the FRS instability peaks at $k = \omega_p/c$ and is distinct from the AMI instability for $Ra_0^2 < (4/3)\omega_p^2/\omega_0^2$. For $Ra_0^2 << (4/3)\omega_p^2/\omega_0^2$ and $k_\perp = 0$, the FRS growth rate at $k = \omega_p/c$ is given by the conventional expression [33-37],

$$\Gamma \cong \frac{a_0}{2\sqrt{2}}\frac{\omega_p^2}{\omega_0}. \tag{19}$$

As Ra_0^2 increases and approaches $(4/3)\omega_p^2/\omega_0^2$ the AMI merges with the FRS instability. For $Ra_0^2 >> (4/3)\omega_p^2/\omega_0^2$ the FRS instability is dominated by the AMI. The ratio of the maximum growth rate for the AMI to the conventional FRS instability is $(3\sqrt{2}/8)Ra_0$. The Raman backscatter instability, on the other hand, is virtually unaffected by the presence of bound electrons, i.e., the Stokes frequency is $\omega = \omega_p$, the wavenumber is $k \cong 2k_0 - \omega_0\omega_p/c^2k_0$, and the growth rate is $\Gamma \cong (\omega_0\omega_p)^{1/2}a_0/2$, assuming $\omega_p/\omega_0 << 1$.

c. Filamentation Instability

As is the case with the modulation and forward Raman instability, the filamentation instability can be strongly affected by bound electrons. Taking $k = 0$ in Eq. (15) and neglecting the resonant plasma wave term, the dispersion relation becomes

$$\omega^2 = 2\omega_0^2\left[1 \pm \left\{\frac{c^2k_\perp^2}{4\omega_0^4}\left(\omega_p^2a_0^2(1+3R/2)/2 - c^2k_\perp^2\right)\right\}^{1/2}\right], \tag{20}$$

where $c^2k_\perp^2 << \omega_0^2$. The AFI growth rate is

$$\Gamma = (ck_\perp/2\omega_0)\left(\omega_p^2a_0^2(1+3R/2)/2 - c^2k_\perp^2\right)^{1/2}, \tag{21}$$

and extends from $k_\perp = 0$ to $k_\perp = k_{\perp max} = (\omega_p a_0 / \sqrt{2}c)(1 + 3R/2)^{1/2}$ and peaks at $k_\perp = k_{\perp max} / \sqrt{2}$. The maximum growth rate for the AFI is

$$\Gamma = (\omega_p^2 a_0^2 / 8\omega_0)(1 + 3R/2), \qquad (22)$$

which is identical to the maximum AMI growth rate in Eq. (18). For R = 0, the growth rate of the conventional RFI for a plasma is recovered [31,33]; whereas for R >> 1, the growth rate of the conventional filamentation instability for a neutral gas is recovered [42]. The ratio of the peak AFI growth rate to the peak RFI growth rate is 3R/2 + 1, which can be much greater than unity.

The effect of the AFI is to transversely break up the laser pulse into filaments, each having a transverse dimension $r_\perp \cong 2/k_\perp$ and a power per filament roughly equal to the critical power. The power per filament is $P = I\pi r_\perp^2 \cong I(4\pi / k_\perp^2) \cong P_p / (1 + 3R/2) \cong P_a$, where $k_\perp = (\omega_p a_0 / 2c)(1 + 3R/2)^{1/2}$ corresponds to the maximum growth rate. This model assumes that the transverse dimension of the laser pulse is greater than $r_\perp$. For the filamentation instability (k = 0), the sideband frequency is purely imaginary, i.e., $\omega^2 < 0$. The instability, therefore, is purely growing in time and does not propagate transversely out of the laser pulse.

d. Examples

Numerical solutions of the full dispersion relation, Eq. (14), are shown in Figs. 1-8, where the normalized growth rate, Γ/ω_p, is plotted versus the normalized wavenumber, ck/ω_p or $ck_\perp/\omega_p$, for various values of the effective R, a_0 and ω_0/ω_p. Figure 1 shows the modulation and Raman growth rate for $k_\perp = 0$, $\omega_0/\omega_p = 10$, $a_0 = 0.01$ ($I = 1.4 \times 10^{14}$ W/cm^2 for $\lambda_0 = 1$ μm) and (a) R = 0 (solid curve), (b) R = 200 (dotted curve) and (c) R = 400 (dashed curve). The solid curve

(R = 0) shows only the conventional FRS instability at $ck/\omega_p = 1$ having a growth rate $\Gamma/\omega_p = 0.7 \times 10^{-3}$, whereas the conventional RMI is not discernible on this plot. The conventional (R = 0) RMI for these parameters has a peak growth rate of $\Gamma/\omega_p = 1.25 \times 10^{-6}$ at $ck/\omega_p \cong 0.05$. For R = 400 (dashed curve) the peak AMI growth rate is $\Gamma/\omega_p = 0.75 \times 10^{-3}$, (3R/2 = 600 times larger than the R = 0 peak value) at $ck/\omega_p \cong 1.3$. The AMI is broadband, extending from $ck/\omega_p = 0$ to 1.7. The peak Raman growth rate for R = 200 is $\Gamma/\omega_p = 0.8 \times 10^{-3}$ and for R = 400 is $\Gamma/\omega_p = 1.0 \times 10^{-3}$, both at $ck/\omega_p = 1$.

Figure 2 shows the modulation and Raman growth rate for $k_\perp = 0$, $\omega_0/\omega_p = 20$, $a_0 = 0.01$ and (a) R = 0 (solid curve), (b) R = 200 (dotted curve) and (c) R = 400 (dashed curve). The solid curve (R = 0) shows only the conventional FRS instability at $ck/\omega_p = 1$ having a growth rate $\Gamma/\omega_p = 0.3 \times 10^{-3}$, whereas the conventional RMI is not discernible on this plot. The peak conventional RMI growth rate is $\Gamma/\omega_p = 0.6 \times 10^{-6}$ at $ck/\omega_p \cong 0.1$. The peak Raman growth rate for R = 200 is $\Gamma/\omega_p = 3 \times 10^{-4}$ and for R = 400 is $\Gamma/\omega_p \cong 3.2 \times 10^{-4}$, both at $ck/\omega_p = 1$. For R = 400 the AMI extends from $ck/\omega_p = 0$ to 3.4 and has a peak growth rate $\Gamma/\omega_p \cong 3.8 \times 10^{-4}$.

Figure 3 shows the modulation and Raman growth rate for $k_\perp = 0$, $\omega_0/\omega_p = 10$, $a_0 = 0.005$ and (a) R = 0 (solid curve), (b) R = 200 (dotted curve) and (c) R = 400 (dashed curve). The solid curve (R = 0) shows only the conventional FRS instability at $ck/\omega_p = 1$ having a growth rate $\Gamma/\omega_p = 4 \times 10^{-4}$, whereas the conventional RMI is not discernible on this plot. The conventional RMI for these parameters has a peak growth rate of $\Gamma/\omega_p = 3.2 \times 10^{-7}$ at $ck/\omega_p \cong 0.025$. For R = 400 (dashed curve) the AMI extends from $ck/\omega_p = 0$ to 0.9 and the peak AMI growth rate is $\Gamma/\omega_p = 2 \times 10^{-4}$ at $ck/\omega_p \cong 0.6$. The peak Raman growth rate for R = 200 is $\Gamma/\omega_p = 4.2 \times 10^{-4}$ and for R = 400 is $\Gamma/\omega_p = 4.5 \times 10^{-4}$, both at $ck/\omega_p = 1$.

Figure 4 shows the modulation and Raman growth rate for $k_\perp = 0$, $\omega_0/\omega_p = 20$, $a_0 = 0.005$ and (a) R = 0 (solid curve), (b) R = 200 (dotted curve) and (c) R = 400 (dashed curve). The solid curve (R = 0) shows only the conventional FRS instability at $ck/\omega_p = 1$ having a growth rate $\Gamma/\omega_p = 1.9 \times 10^{-4}$, whereas the conventional RMI is not discernible on this plot. The conventional RMI for these parameters has a peak growth rate of $\Gamma/\omega_p = 1.5 \times 10^{-7}$ at $ck/\omega_p \cong 0.05$. For R = 400 (dashed curve) the AMI extends from $ck/\omega_p = 0$ to 1.7 and the peak AMI growth rate is Γ/ω_p =

1×10^{-4}, at $ck/\omega_p \cong 1.2$. The peak Raman growth rates for R = 200 and for R = 400 are approximately the same and equal to $\Gamma/\omega_p = 2 \times 10^{-4}$, with both peaks at $ck/\omega_p = 1$.

Figure 5 shows the filamentation growth rate for k = 0, $\omega_0/\omega_p = 10$, $a_0 = 0.01$ and (a) R = 200 (dotted curve) and (b) R = 400 (dashed curve). The conventional RFI is not discernible on this plot. The conventional RFI for these parameters with R = 0 has a peak growth rate of $\Gamma/\omega_p = 1.3 \times 10^{-6}$ at $ck_\perp/\omega_p \cong 0.005$. For R = 400 (dashed curve) the peak AFI growth rate is $\Gamma/\omega_p = 8 \times 10^{-4}$ at $ck_\perp/\omega_p \cong 0.13$.

Figure 6 shows the filamentation growth rate for k = 0, $\omega_0/\omega_p = 20$, $a_0 = 0.01$ and (a) R = 200 (dotted curve) and (b) R = 400 (dashed curve). The conventional RFI, which is not discernible on this plot, has a peak growth rate of $\Gamma/\omega_p = 6 \times 10^{-7}$ at $ck_\perp/\omega_p \cong 0.005$. For R = 400 (dashed curve) the peak AFI growth rate is $\Gamma/\omega_p = 3.9 \times 10^{-4}$, at $ck_\perp/\omega_p \cong 0.13$.

Figure 7 shows the filamentation growth rate for k = 0, $\omega_0/\omega_p = 10$, $a_0 = 0.005$ and (a) R = 200 (dotted curve) and (b) R = 400 (dashed curve). The conventional RFI, which is not discernible on this plot, has a peak growth rate of $\Gamma/\omega_p = 3 \times 10^{-7}$ at $ck_\perp/\omega_p \cong 0.0025$. For R = 400 (dashed curve) the peak AFI growth rate is $\Gamma/\omega_p = 1.9 \times 10^{-4}$, at $ck_\perp/\omega_p \cong 0.06$.

Figure 8 shows the filamentation growth rate for $k = 0$, $\omega_0/\omega_p = 20$, $a_0 = 0.005$ and (a) $R = 200$ (dotted curve) and (b) $R = 400$ (dashed curve). The conventional RFI, which is not discernible on this plot, has a peak growth rate of $\Gamma/\omega_p = 1.5 \times 10^{-7}$ at $ck_\perp/\omega_p \cong 0.0025$. For $R = 400$ (dashed curve) the peak AFI growth rate is $\Gamma/\omega_p = 9.5 \times 10^{-5}$, at $ck_\perp/\omega_p \cong 0.06$.

Figures 9-12 show surface plots of the normalized growth rate, Γ/ω_p, as a function of ck/ω_p and $ck_\perp/\omega_p$ for various values of R, a_o and ω_0/ω_p. These surface plots are useful since they display simultaneously the growth rates corresponding to the modulational, Raman and filamentation instabilities. In Fig. 9, $\omega_0/\omega_p = 10$, $a_0 = 0.01$ and (a) $R = 200$ and (b) $R = 400$, as is the case in the one-dimensional plots of Figs. 1 and 5. The surface plot corresponding to the conventional $R = 0$ limit, which is not shown, is dominated by the very narrow peak of the Raman instability in the vicinity of $ck/\omega_p \cong 1$. Similarly, Figs. 10,11 and 12 are surface plots for $\omega_0/\omega_p = 10$, $a_0 = 0.005$, $\omega_0/\omega_p = 20$, $a_0 = 0.01$, and $\omega_0/\omega_p = 20$, $a_0 = 0.005$, respectively, with (a) $R = 200$ and (b) $R = 400$. All the surface plots display the Raman peak near $ck/\omega_p = 1$, however, the peak of the Raman instability is not fully resolved due to the coarse grid used in these plots. Figures

9-12 clearly indicated that as R is increased the AMI and AFI growth rates increase and, for sufficiently large R, dominate over the conventional RMI, FRS and RFI.

e. Physical Mechanism of Modulational Instability

The physical mechanism for the modulational instability is due to group velocity dispersion (GVD) and self-phase modulation (SPM). Dispersion is dominated by the plasma electrons, which provide "anomalous" GVD, and the nonlinearity is dominated by the bound

electrons, which provide SPM. These are the two necessary ingredients for a modulation instability [46]. The group velocity can be written as $v_g \cong v_{g0} + \delta v_g$, where $v_{g0} = c\left(1 - (\omega_p^2 + c^2 k_{\perp 0}^2)/\omega_0^2\right)^{1/2}$ is the linear group velocity, $\delta v_g \cong c\left((\omega_p^2 + c^2 k_{\perp 0}^2)/\omega_0^2\right)\delta\omega/\omega_0$ is the perturbed nonlinear group velocity and $\delta\omega$ is the nonlinear frequency shift. Note that higher frequencies have higher group velocity, i.e., anomalous GVD. Here, the effects of a finite transverse wavenumber $k_{\perp 0} = 2/r_0$ associated with the pump wave have been included, which can also result in anomalous GVD. The SPM process is responsible for the nonlinear frequency shift, which is proportional to the nonlinear index times the gradient of the intensity, i.e., $\eta_2 \nabla(a^2)$. In a frame of reference moving with the linear group velocity v_{g0}, consider a spatially localized perturbation in the field amplitude, $a = a_0 + \delta a$, where $\delta a > 0$, as indicated in Fig. 13. The perturbed amplitude will produce a local frequency shift through the SPM and hence a perturbed nonlinear group velocity δv_g. The rate of change of the nonlinear frequency shift is $\partial\delta\omega/\partial t = c(\omega_p^2/4\omega_0)R\partial(a^2)/\partial\xi \approx c(\omega_p^2/2\omega_0)Ra_0\partial\delta a/\partial\xi$, where $\xi = z - v_{g0}t$ is the axial position in the group velocity frame. If the perturbation δa is peaked around $\xi = 0$, then the frequency just ahead of the perturbation ($\xi > 0$) is decreased (red shifted) and is increased (blue shifted) just behind the perturbation ($\xi < 0$). Since δv_g is proportional to $\delta\omega$, $\delta v_g < 0$ just ahead of the perturbation and $\delta v_g > 0$ just behind the perturbation. Hence, energy flows towards the positive perturbation at $\xi = 0$ and δa grows. The rate of increase in the perturbed amplitude is $\partial\delta a/\partial t \cong -(a_0/2)\partial\delta v_g/\partial\xi = -(a_0/2)\left((\omega_p^2 + c^2 k_{\perp 0}^2)/\omega_0^2\right)(c/\omega_0)\partial\delta\omega/\partial\xi$. Operating on this relationship with $\partial/\partial t$ and using the above expression for $\partial\delta\omega/\partial t$ we find that

$\partial^2 \delta a / \partial t^2 = -(c^2/4)\left((\omega_p^2 + c^2 k_{\perp 0}^2)/\omega_0^2\right)(\omega_p/\omega_0)^2 \, Ra_0^2 \partial^2 \delta a / \partial \xi^2$. Replacing $\partial^2/\partial t^2$ with Γ^2 and $\partial^2/\partial \xi^2$ with $-k^2$ we find that

$$\Gamma \cong \left((\omega_p^2 + c^2 k_{\perp 0}^2)^{1/2}/\omega_0\right)(\omega_p/\omega_0) R^{1/2} a_0 ck/2,$$

which agrees with the expression obtained in Eq. (17), to within a factor of order unity, when $k_{\perp 0} = 0$ and $k = (3/8)^{1/2} a_0 R^{1/2} \omega_0/c$, which is the wavenumber corresponding to the maximum growth. The AMI requires free electrons and/or a sufficiently large $k_{\perp 0}$. In the absence of free electrons a gas usually has normal GVD ($\partial v_g / \partial \omega < 0$) for $k_{\perp 0} = 0$ and the AMI is stable. The GVD due to bound electrons can be neglected compared to that of the free electrons. Group velocity dispersion [46] is measured by the parameter $\beta_2 = c^{-1}\partial^2(\omega_0 \eta)/\partial^2 \omega_0$. The plasma contribution to β_2 is $\beta_{2p} = -(\omega_p/\omega_0)^2/(c\omega_0) \cong -10^{-28}$ sec^2/cm (for $\omega_0/\omega_p \cong 10$ and $\lambda_0 \cong 1$ μm) and is typically opposite in sign and 10^3 times greater in magnitude than the contribution from usual gases at STP, as discussed in Appendix A.

V. Discussion and Conclusion

The presence of bound electrons in a partially-stripped plasma can significantly alter the propagation and stability of laser pulses. A partially-stripped plasma will result when a plasma is formed from a relatively high-Z material, e.g., the photo-ionization of nitrogen, argon, or krypton; or by exploding a metallic foil or wire. This is the case in many experiments on x-ray lasers, high-order harmonic generation, and in laser-channeling experiments for laser accelerators and laser-fusion. In such a plasma, the optical nonlinearities can be completely dominated by bound electron effects. In particular, the ratio of the third-order nonlinearity for free electrons to that of bound electrons is given by the ratio of critical powers for self-focusing, $R = P_p/P_a$, which

is typically much greater than unity. Growth rates for various instabilities have been obtained in terms of the effective value of R for a partially-stripped atom.

When $R >> 1$, the combination of anomalous GVD from the free electrons and SPM from the bound electrons leads to a strong instability, i.e., the AMI. In a fully-stripped plasma, modulational-type instabilities are dominated by FRS, which occurs in a narrow band around $\omega = \omega_p$ and $k = \omega_p/c$. In the presence of bound electrons, however, the growth rate of the AMI can be greater than that of FRS and occurs at a much higher and broader range of ω and k. This implies that axial breakup of a laser will occur much more rapidly in a partially-stripped plasma and, due to the large range of unstable ω and k, the instability will be less sensitive to variations in the ambient density or to laser incoherence effects. When $R >> 1$, the transverse breakup of the laser pulse is dominated by the AFI. Provided the laser power greatly exceeds P_a, the laser pulse will form transverse filaments with a power per filament on the order of P_a.

The present analysis contains a number of assumptions. In particular, the laser pulse length must be sufficiently short and the intensity must be sufficiently low so that further ionization of the plasma is avoided. These requirements can be easily met, given the availability of ultrashort (< 1 ps) high power lasers and the high binding energies of inner shell electrons. Perhaps a more stringent constraint on the laser intensity is the validity of the polarization field expansion $\underset{\sim}{P} = (\chi^{(1)} + \chi^{(3)}\, \underset{\sim}{E} \bullet \underset{\sim}{E})\, \underset{\sim}{E}$, which assumes $\eta_0 - 1 >> \eta_2 I$. Inclusion of bound electron effects could alter the interpretation of laser interaction experiments with high-Z material.

Acknowledgments

One of us (PS) would like to thank S.E. Harris for many stimulating and useful discussions. The authors also acknowledge useful conversations with J. Reintjes, A. Ting,

R. Lehmberg, P. Shkolnikov, G. Joyce, W. Manheimer, and S. Bodner. This work was supported by the Office of Naval Research and the Department of Energy.

Appendix A: Nonlinear Susceptibility and GVD Parameter

a. Nonlinear Susceptibility

A rough estimate for $\chi^{(3)}$ and η_2 far from any atomic resonances can be obtained by equating the linear and nonlinear polarization fields and setting the electric field equal to the characteristic atomic (hydrogenic) field $E_a = q / r_B^2 = 5.2 \times 10^9 V / cm$, where $r_B = \hbar^2 / q^2 m$ is the Bohr radius [42-44]. Note that the intensity of a linearly polarized laser pulse with a peak field equal to E_a is $I = (c / 8\pi)E_a^2 \cong 3.6 \times 10^{16} W / cm^2 (a_0 = 0.16 \text{ for } \lambda_0 = 1\ \mu m)$. The magnitude of the third order susceptibility is, therefore, approximately $\chi^{(3)} \cong \chi^{(1)} / E_a^2 = \chi^{(1)} r_B^4 / q^2$. Since $4\pi\chi^{(1)}$ is unitless, of order unity for condensed matter (density $\sim 2 \times 10^{22}$ cm^{-3}) and proportional to the density, we can write $\chi^{(1)} \cong 4 \times 10^{-24} n_a\ [cm^{-3}]$. Hence, order of magnitude estimates for $\chi^{(3)}$ and η_2 are $\chi^{(3)}[esu] \cong 10^{-38} n_a[cm^{-3}]$ and $\eta_2\ [cm^2/W] \cong 5 \times 10^{-40} n_a[cm^{-3}]$, where $\chi^{(3)}[esu]$ is in units of $(cm/statvolts)^2$. Table I lists the approximate measured values for the third order susceptibility for various gases at STP and for linearly polarized 0.5 μm radiation [19,42]. Also listed in Table I are the nonlinear focusing power in a gas P_a and the ratio of the critical powers for relativistic plasma focusing and nonlinear gas focusing $R = P_p/P_a$. The value of η_2, defined by $\Delta\eta_a = \eta_2 I$, in units of cm^2/W can be obtained by multiplying the value of $\chi^{(3)}$ in esu by $0.0395/\eta_0^2$.

The nonlinear susceptibility $\chi^{(3)}$ for an ionized atom can be simply estimated if the charge state is small compared to the atomic number and the optical frequency is far below any atomic resonance. The nonresonant nonlinear susceptibility is approximately given by $\chi^{(3)} \cong 8 n_a \mu^4 / \hbar^3 \Omega_R^3$, where $\mu \cong q r_B$ is the typical dipole moment and Ω_R is the typical value of

the atomic resonance frequency [44]. Since Ω_R is roughly proportional to the ionization potential U_I, the ratio of the nonlinear susceptibilities of the ionized atom to the neutral atom is

$$\chi_+^{(3)} / \chi^{(3)} \approx (U_I / U_I^+)^3, \tag{A1}$$

where U_I^+ is the ionization potential for the ionized atom. As an example, for Xe gas, $U_I = 12.1$ eV, $U_I^+ = 21.2$ eV (for the singly-ionized state), and $\chi_+^{(3)} / \chi^{(3)} \cong 0.18$.

b. Dispersion Parameter for Free and Bound Electrons

In Secs. II-IV, the frequency dependence of $\chi^{(1)}$ was neglected in the derivation of the dispersion relation. This is justified since dispersion is dominated by the free electrons and not the bound electrons. Dispersion is determined by the frequency dependence of the linear refractive index, $\eta_L = \eta_0 + \eta_{Lp}$, where η_0 is the bound electron contribution and η_{Lp} is the plasma (free electron) contribution. An order of magnitude estimate of η_0 far below any resonance is given by the simple model

$$\eta_0 \cong 1 + \frac{\omega_a^2}{\Omega_R^2 - \omega_0^2} \cong 1 + \frac{\omega_a^2}{\Omega_R^2}\left(1 + \frac{\omega_0^2}{\Omega_R^2}\right), \tag{A2}$$

where $\omega_a^2 = 4\pi n_a q^2 / m$, n_a is the density of atoms, $\Omega_R \cong 10^{16}$ sec^{-1} is a typical value of the atomic resonance frequency, and $\omega_a^2 << \omega_0^2 << \Omega_R^2$ is assumed [42-44]. For a plasma,

$$\eta_{Lp} \cong 1 - \omega_p^2 / 2\omega_0^2, \tag{A3}$$

where $\omega_p^2 / \omega_0^2 << 1$ is assumed [35]. Lowest order dispersion is characterized by the group velocity dispersion (GVD) parameter $\beta_2 = c^{-1}\partial^2(\omega_0\eta_L) / \partial\omega_0^2$ [46]. For a neutral gas $\beta_{2a} = c^2(\omega_0\eta_0) / \partial^2\omega_0 \cong 6\omega_a^2\omega_0 / c\Omega_R^4$, whereas for a plasma

$\beta_{2p} = c^2(\omega_0 \eta_{Lp})\partial^2\omega_0 \cong -\omega_p^2 / c\omega_o^3$. Note that $\beta_{2a} > 0$ and $\beta_{2p} < 0$, i.e., the GVD is "normal" for a neutral gas (below resonance) and "anomalous" for a plasma. The ratio of the dispersion parameter for a neutral gas to that of a plasma is,

$$\beta_{2a} / \beta_{2p} = -6(n_a / n_p)(\omega_0 / \Omega_R)^4, \qquad \text{(A4)}$$

and, typically, $|\beta_{2a}/\beta_{2p}| << 1$, since $\omega_0/\Omega_R << 1$. For example, $\beta_{2p} \cong -10^{-28}$ sec^2/cm for $\lambda_0 = 1$ μm and $\omega_0/\omega_p = 10$ ($n_p \cong 10^{19}$ cm^{-3}); whereas $\beta_{2a} \cong 10^{-31}$ sec^2/cm for air at STP and $\lambda_0 = 1$ μm.

Appendix B: Ionization Rates

The rate of change of plasma density (density of free electrons) is given by

$$\frac{\partial n_p}{\partial t} = W_p n_a + W_c n_p - \nu_r n_p, \tag{B1}$$

where W_p is the photoionization rate, W_c is the collisional ionization rate, and ν_r is the recombination rate. Typically, for parameters of interest here, the recombination rate is small compared to the collisional ionization rate, i.e., $\nu_r << W_c$, and will be neglected. The solution of Eq. (B1) for constant ionization rates is

$$n_p = (W_p / W_c) n_a \left(\exp(W_c t) - 1\right) + n_{p0} \exp(W_c t), \tag{B2}$$

where n_{p0} is the initial (seed) electron density and it is assumed that the plasma density remains small compared to the neutral density. However, both W_p and W_c are functions of time as will be discussed.

a. Photoionization

Photoionization can take place in either the tunneling or multiphoton regime [47-52]. These regimes are characterized by the Keldysh parameter $\gamma_k = (U_I / U_{0s})^{1/2}$, where U_I is the ionization energy and $U_{0s} = (1/2)m(qE_0/m\omega_0)^2$ is the electron oscillation energy. The Keldysh parameter can also be written as $\gamma_k = \omega_0 \tau_t$, where τ_t is the tunneling time, i.e., the transit time of the electron through the atomic Coulomb barrier. The low field limit ($\gamma_k > 1$) corresponds to the multiphoton ionization regime, whereas the high field limit ($\gamma_k < 1$) corresponds to the tunneling ionization regime.

(i) Tunneling Ionization ($\gamma_k < 1$)

In the high field limit, $\gamma_k < 1$, the photoionization rate can be determined by a tunneling calculation for an atom in the presence of a static electric field of amplitude E. The tunneling ionization rate, i.e., the probability (per unit time) of ionization, is given by [47,48]

$$W_t = A_g \tilde{E}^{-1/2} \exp(\beta_g / \tilde{E}), \qquad \text{(B3)}$$

where $A_g = 1.6 \times 10^{17} \tilde{U}_I^{7/4}$, $\beta_g = 0.67 \tilde{U}_I^{3/2}$, $\tilde{U}_I = U_I / U_H$ is the normalized ionization energy, U_I is the ionization energy in eV, $U_H = 13.6$ eV, $\tilde{E} = E_0/E_a$ is the normalized electric field, and W_t is in units of sec^{-1}. Figure 14 shows the tunneling ionization time, $1/W_t$, as a function of laser intensity for various values of ionization energy. For a laser intensity of 10^{15} W/cm^2 and ionization energy of 50 eV, the tunneling ionization time is ~ 100 nsec. For laser pulse durations much less than 100 nsec, little tunneling ionization will occur for these parameters.

(ii) Multiphoton Ionization ($\gamma_k > 1$)

In the low field limit, $\gamma_k > 1$, the photoionization rate is given by the multiphoton ionization rate, which is proportional to I^m, where I is the laser intensity and m = integer $(U_I / \hbar\omega_0 + 1)$ is the number of absorbed photons necessary for ionization. The multiphoton ionization rate is given by [50-52]

$$W_m = (\sigma I / \hbar\omega_0^2)^m (2\pi\omega_0 / (m-1)!), \qquad \text{(B4)}$$

where $\sigma = 10^{-16}$ cm^2.

b. Collisional Ionization

In an oscillating electric field an electron, on average, gains energy from the field provided there are collisions with other particles. In the classical description, this is referred to as Joule heating; in the quantum picture, this is called inverse bremsstrahlung. An electron that gains sufficient energy from the field can ionize an atom on collision, leading to additional free electrons, which can go through the same cycle. In the collisional ionization process, the presence of seed electrons is necessary. If the irradiated volume is small, or if the gas is sufficiently tenuous, the seed electrons must be provided by other means. For example, the initial electrons may come from tunneling ionization, or from cosmic ray ionization.

The collisional ionization rate will be discussed in two limits: the low intensity limit $U_{os} < U_I$ and the high intensity limit $U_{os} >> U_I$. In the low intensity limit $U_{os} < U_I$, an electron oscillating in the laser field with energy U_{os} does not have sufficient energy to ionize an atom in a single collision. Through multiple collisions, however, the electron energy can increase beyond U_I and collisional ionization can occur. In the limit $U_{os} >> U_I$, an electron has a sufficiently high energy to directly ionize the atom. Furthermore, in the limit $U_{os} >> U_I$, the electron-neutral collision frequency becomes Coulomb-like. Before discussing the collisional ionization rate in the low and high intensity limits, the momentum transfer collision frequency, which is needed to obtain the collisional ionization rates, will be discussed.

(i) Momentum Transfer Collision Frequency

As the electrons in the ionized gas oscillate under the influence of the laser field, they collide with the background electrons, ions, and neutral atoms. The electron collision frequency for momentum transfer is

$$\nu_m = \nu_{ei} + \nu_{en}, \tag{B5}$$

where ν_{ei} (ν_{en}) is the electron-ion (electron-neutral) collision frequency. The electron-electron collision frequency does not contribute to ν_m because the momentum of any pair of colliding electrons and associated current (masses and charges are identical) are conserved. Electron-electron collisions, however, lead to thermalization of the electrons.

The electron-ion collision frequency is given by [53]

$$\nu_{ei}[\sec^{-1}] = 4 \times 10^{-6} \ell n\Lambda_{ei} n_i[cm^{-3}] \overline{Z}^2 U_{os}^{-3/2}[eV], \tag{B6}$$

where $\ell n\Lambda_{ei}$ is the Coulomb logarithm (typically, $\ell n\Lambda_{ei} \cong 10 - 20$), $\overline{Z}$ is the charge state and n_i is the ion density ($n_i \overline{Z}$ is the electron plasma density).

The electron-neutral collision frequency is given by [54-56]

$$\nu_{en} = \langle v_e n_n \sigma_{en}(v) \rangle, \tag{B7}$$

where σ_{en} is the electron-neutral cross section, v_e is the electron velocity, and the brackets $< >$ denote an averaging over the electron velocity distribution. The electron-neutral cross section is generally a complicated function of the electron velocity. At low electron velocities the cross section is hard-sphere-like and independent of velocity, $\sigma_{en} \cong \sigma_0$, where $\sigma_0 \sim 10^{-15}$ cm^2 is the hard-sphere cross section. As the electron velocity approaches the characteristic atomic electron velocity , polarization scattering is the dominant process and $\sigma_{en} \cong \sigma_0 v_0 / v_e$. The characteristic atomic electron velocity is $v_0 = \alpha_f c$, where $\alpha_f = 1/137$ is the fine-structure constant and the characteristic electron energy is $m v_0^2 / 2 = 13.6$ eV. At substantially higher electron velocities the scattering becomes Coulomb-like and $\sigma_{en} \sim 1 / v_e^4$. The electron-neutral

collision frequency can therefore be estimated to be $\nu_{en} \cong n_n \sigma_0 v_{os}$ for $v_{os} < v_0$ and $\nu_{en} \cong n_n \sigma_0 v_o$ for $v_{0s} > v_0$.

Typically, the electron-neutral collisions are the dominant collisional process in weakly ionized gases; however, in highly ionized gases ν_{ei} can become important. As an example, consider the case where the neutral density is $n_{n0} = 3 \times 10^{19}$ cm^{-3} and the electron oscillation velocity is $v_{0s} = qE_0/m\omega_0 = 5 \times 10^{-3} c$ ($U_{0s} = mv_{os}^2 / 2 = 6.3$ eV). For a linearly polarized laser of wavelength $\lambda = 1$ μm, these parameters correspond to a peak intensity of $I = 3.5 \times 10^{13}$ W/cm^2 and peak electric field amplitude of $E_0 = 1.6 \times 10^8$ V/cm. Taking $\sigma_0 \cong 10^{-15}$ cm^2, Eq. (B7) yields an electron-neutral collision frequency of $\nu_{en} \cong 7 \times 10^{12}$ sec^{-1}, i.e., an electron-neutral collision time of $\tau_{cn} = \nu_{en}^{-1} \sim 140$ fsec.

If, for the same example, the gas is highly ionized with $n_i = n_{n0} = 3 \times 10^{19}$ cm^{-3} and the electron oscillation energy is $U_{0s} = 6.3$ eV, the electron-ion collision frequency from Eq. (B6) for singly ionized gas ($\bar{Z} = 1$) is $\nu_{ei} \cong 8 \times 10^{13}$ sec^{-1}, i.e., an electron-ion collision time of $\tau_{ei} = \nu_{ei}^{-1} \cong 13$ fsec. For these parameters the electron-ion collision frequency is much greater than the electron-neutral collision frequency, $\nu_{ei} >> \nu_{cn}$.

As another example consider the case of a plasma in which all the atoms are singly ionized, i.e., $\bar{Z} = 1$. For a laser intensity of $I = 10^{16}$ W/cm^2 and wavelength $\lambda_0 = 1$ μm, the electron oscillation energy is $U_{os} \cong 2$ keV. For an ion density of $n_i = 3 \times 10^{19}$ cm^{-3}, the electron-ion collision frequency is $\nu_{ei} \cong 1.2 \times 10^{10}$ sec^{-1} and $\tau_{ei} = \nu_{ei}^{-1} \cong 80$ psec.

(ii) Collisional Ionization Rate for $U_{os} < U_I$

The collisional ionization rate is

$$W_c(t) = n_a \int_{v_I}^{\infty} \sigma_c(v) v f_e(v,t) dv, \tag{B8}$$

where n_a is the density of atoms (neutrals), $\sigma_c(v)$ is the ionization cross section for electron impact, $f_e(v,t)$ is the electron distribution function, with $\int_0^{\infty} f_e(v,t)dv = 1$, and $v_I = (2U_I / m)^{1/2}$ is the velocity associated with ionization [52,54-56]. The collisional ionization cross section, as a function of electron energy, is typically zero from $U = 0$ to $U = U_I$, increases from U_I to U_m, where U_m is several times U_I, and then decreases as $\sim 1/U$ for $U >> U_m$. Order of magnitude estimates for the collisional ionization cross section for a neutral gas can be obtained from the following three parameter model

$$\sigma_c = \sigma_m \alpha_0^2 \frac{U_I(U - U_I)}{U(U + U_0)}, \tag{B9}$$

for $U > U_I$ and $\sigma_c = 0$ for $U < U_I$, where σ_m is the maximum cross section occurring at $U = U_m = \alpha_0 U_I$, U_I is the ionization energy, $U_0 = \alpha_0(\alpha_0 - 2)U_I$ and α_0 is a parameter. Approximate values [57,58] for U_I, σ_m and α_0 are given in Table II for H_2, N, N_2 and Ar.

As a rough estimate we take the electron distribution to be a flat top of the form,

$$f_e(v,t) = \begin{cases} 1 / v_e(t), & 0 \le v \le v_e \\ \\ 0, & v > v_e, \end{cases} \tag{B10}$$

where $v_e(t)$ is the maximum electron velocity which evolves with time. Substituting (B10) into (B8) gives

$$W_c(t) = n_a \int_{v_I}^{v_e} \sigma_c(v)\left(v / v_e(t)\right) dv, \tag{B11}$$

for $v_e(t) > v_I$ and $W_c(t) = 0$ for $v_e(t) < v_I$. Substituting Eq. (B9) into (B11) gives the collisional ionization rate,

$$W_c(t) = n_a \sigma_m \alpha_0 \left(\frac{U_I}{2m}\right)^{1/2} \left(U_I / U_e(t)\right)^{1/2} F\left(U_e(t),\, U_I,\, \alpha_0\right), \tag{B12}$$

for $U_e(t) > U_I$ and $W_c(t) = 0$ for $U_e(t) < U_I$, where

$$F(U_e(t),\, U_I,\, \alpha_0) = (1 + U_I / U_0)\ell n\left(\frac{U_e(t) + U_0}{U_I + U_0}\right) - \frac{U_I}{U_0}\ell n\left(\frac{U_e(t)}{U_I}\right), \tag{B13}$$

and $U_e(t) = mv_c^2 / 2$ is the electron energy.

The rate of change of energy of an electron undergoing collisions in the presence of a temporally periodic electric field is given by [54,55]

$$\frac{dU_e}{dt} = \frac{q^2 E^2 \nu_m}{2m(\omega_0^2 + \nu_m^2)} - \nu_u U_e, \tag{B14}$$

where E is the peak electric field amplitude, ν_m is the momentum transfer frequency, and ν_u is the energy exchange collision frequency. The first term on the right-hand side of Eq. (B14) represents the rate of energy increase of an electron undergoing collisions while being accelerated in the laser field. The second term represents the energy damping due to collisions between electrons and neutral atoms. In light gases, such as helium, a rough estimate for the exchange collision frequency is $\nu_u \cong (2m/M)\nu_m$, where M is the mass of the atom, however, actual values can be substantially higher than this estimate. As a specific example, for electron energies between $U_e \cong 10^{-2}$ eV and 2 eV the momentum collision frequency for N_2 is $\nu_m[\text{sec}^{-1}] \cong 10^{-7} n_n (U_e[\text{eV}])^{0.85}$ and the energy exchange collision frequency is, to within an order of magnitude, $\nu_u \cong \nu_m/100$.

Equation (B14) indicates that the electron energy increases monotonically and saturates because of electron collisions with neutral atoms. Solving Eq. (B14), assuming ν_m and ν_u are constant, gives

$$U_e(t) = U_{sat}\left(1 - \exp(-\nu_u t)\right), \qquad \text{(B15)}$$

where $U_{sat} = \left(\nu_m / \nu_u\right)\left(1 + \nu_m^2 / \omega_0^2\right)^{-1} U_{0s}$ is the saturation (maximum) electron energy, $U_{0s} = mv_{0s}^2 / 2$ is the electron oscillation energy and $v_{0s} = qE/m\omega_0$ is the oscillation velocity.

Figure 15 shows the collisional ionization time $1/W_c$ as a function of time for $U_I = 20$ eV for (a) $I = 10^{14}$ W/cm^2 (dashed), (b) $I = 10^{13}$ W/cm^2 (dotted) and (c) $I = 5 \times 10^{12}$ W/cm^2 (solid). The collisional ionization time is relatively long for short times, decreases and eventually tends to a constant value as $U_e \rightarrow U_{sat}$. If we regard the abscissa as the laser pulse duration, then, for $I = 5 \times 10^{12}$ W/cm^2, the plasma density e-folding time ($1/W_c$) is long compared to the laser pulse duration provided that the laser pulse duration is $\lesssim$ 10 ps.

(iii) Collisional Ionization Rate for $U_{0s} >> U_I$

Next we consider the regime where $U_{0s} >> U_I$ and the electron-atom collision is Coulomb-like. To estimate the collisional ionization rate in this regime we set the rate of energy loss of a fast electron undergoing collisions with atomic electrons equal to the ionization rate W_c times the effective ionization energy. The rate of energy loss of a fast electron with velocity v_e as it undergoes collisions with background atomic electrons is [59,60]

$$dU_e / dt \cong -\nu_{ee} U_e, \qquad \text{(B16)}$$

where

$$\nu_{ee} = 2\sqrt{2}\pi Z n_a q^2 \ell n\Lambda (m U_e^3)^{-1/2}, \qquad \text{(B17)}$$

is the electron-electron energy exchange frequency, Z is the atomic number, n_a is the atomic density, i.e., Zn_a is the bound electron density, and $\ell n\Lambda$ is the Coulomb logarithm (typically $\ell n\Lambda \sim 10$). In practical units ν_{ee} is

$$\nu_{ee}[\sec^{-1}] = 7.8 \times 10^{-6} Z n_a[\mathrm{cm}^{-3}] \ell n\Lambda (U_e[\mathrm{eV}])^{-3/2}. \qquad \text{(B18)}$$

The collisional ionization rate is estimated by setting dU_e/dt in Eq. (B16) equal to $-W_c \alpha U_I$, which gives $W_c = (U_e/\alpha U_I)\nu_{ee}$, where αU_I is the effective ionization energy, U_I is the ionization energy and $\alpha \cong 2$ to 5 is a numerical factor which accounts for the fact that not all of the fast electron energy loss goes into ionizing the atomic electrons. Solving for W_c and setting $U_e = U_{0s}$ and $\alpha = 3$ we find that the collisional ionization rate for $U_{0s} >> U_I$ is

$$W_c[\sec^{-1}] \cong 2.6 \times 10^{-6} Z n_a[\mathrm{cm}^{-3}] \ell n\Lambda \left(U_{0s}^{1/2}[\mathrm{eV}] U_I[\mathrm{eV}]\right)^{-1}. \qquad \text{(B19)}$$

The collisional ionization time $1/W_c$ in the high energy limit, Eq. (B19), is shown in Fig. 16 for (a) $U_I = 20$ eV, (b) $U_I = 50$ eV and (c) $U_I = 100$, as a function of laser intensity. Figure 16 shows that $1/W_c$ increases with both U_i and I, as expected from Eq. (B19).

References

1. N.H. Burnett and P.B. Corkum, J. Opt. Soc. Am. B 6, 1195 (1989); P. Amendt, D.C. Eder, and S.C. Wilks, Phys. Rev. Lett. 66, 2589 (1991).

2. S. Suckewer and C.H. Skinner, Science 247, 1553 (1990); P. Eisenberger and S. Suckewer, Science 274, 201 (1996); K.M. Krushelnick, W. Tighe, and S. Suckewer, J. Opt. Soc. Am. B 13, 306 (1996).

3. D.C. Eder, P. Amendt, L.B. DaSilva, R.A. London, B.J. MacGowan, D.L. Matthews, B.M. Penetrante, M.D. Rosen, S.C. Wilks, T.D. Donnelly, R.W. Falcone, and G.L. Strobel, Phys. Plasmas 1, 1744 (1994).

4. B.E. Lemoff, G.Y. Yin, C.L. Gordon III, C.P.J. Barty, and S.E. Harris, Phys. Rev. Lett. 74, 1574 (1995).

5. T. Ditmire, T. Donnelly, R.W. Falcone, and M.D. Perry, Phys. Rev. Lett. 75, 3122 (1995).

6. M. Tabak, J. Hammer, M.E. Glinsky, W.L. Kruer, S.C. Wilks, J. Woodworth, E. M. Campbell, and M. D. Perry, Phys. Plasma 1, 1626 (1994).

7. N.D. Delamater, T.J. Murphy, A.A. Hauer, R.L. Kauffman, A.L. Richard, E.L. Lindman, G.R. Magelssen, B.H. Wilde, D.B. Harris, B.A. Failor, J. Wallace, L.V. Powers, S.M. Pollaine, L.J. Suter, R. Chrien, T.D. Shepard, H.A. Rose, E.A. Williams, M.B. Nelson, M.D. Cable, J.B. Moore, M.A. Salazar, and K. Gifford, Phys. Plasmas 3, 2022 (1996).

8. C.J. Pawley, et al, Phys. Plasmas (May 1997 in press).

9. P. Sprangle, E. Esarey, A. Ting, and G. Joyce, Appl. Phys. Lett. 53, 2146 (1988); E. Esarey, A. Ting, P. Sprangle, and G. Joyce, Comments Plasma Phys. Controlled Fusion 12, 191 (1989).

10. P. Sprangle, E. Esarey, and A. Ting, Phys. Rev. Lett. 64, 2011 (1990); Phys. Rev. A 41, 4463 (1990).

11. P. Sprangle, E. Esarey, J. Krall, and G. Joyce, Phys. Rev. Lett. 69, 2200 (1992); E. Esarey, P. Sprangle, J. Krall, A. Ting, and G. Joyce, Phys. Fluids B 5, 2690 (1993).

12. N.E. Andreev, L.M. Gorbunov, V.I. Kirsanov, A.A. Pogosova, and R.R. Ramazashvili, JETP Lett. 55, 571 (1992).

13. C.E. Clayton, K.A. Marsh, A. Dyson, M. Everett, A. Lal, W.P. Leemans, R. Williams, and C. Joshi, Phys. Rev. Lett. 70, 37 (1993); C.E. Clayton, M.J. Everett, A. Lal, D. Gordon, K.A. Marsh, and C. Joshi, Phys. Plasmas 1, 1753 (1994).

14. A. Modena, Z. Najmudin, A.E. Dangor, C.E. Clayton, K.A. Marsh, C. Joshi, V. Malka, C.B. Darrow, C. Danson, D. Neely, and F.N. Walsh, Nature 377, 606 (1995).

15. D. Umstadter, S.-Y. Chen, A. Maksimchuk, G. Mourou, and R. Wagner, Science 273, 472 (1996).

16. A. Ting, C.I. Moore, K. Krushelnick, c. Manka, E. Esarey, P. Sprangle, R. Hubbard, H.R. Burris, R. Fischer, and M. Baine, Accepted for publication in Phys. Plasmas (1997).

17. C.D. Decker, W.B. Mori, K.-C. Tzeng, and T. Katsouleas, Phys. Plasmas 3, 2047 (1996).

18. E. Esarey, P. Sprangle, J. Krall, and A. Ting, IEEE Trans. Plasma Sci. PS-24, 252 (1996).

19. A. L'Huillier, L.A. Lompre, G. Mainfray, and C. Manus, in Atoms in Intense Laser Fields, edited by M. Gavrila (Academic, San Diego, 1992), p. 139.

20. J. Macklin, J. Kmetec, and C. Gordon, Phys. Rev. Lett. 70, 760 (1993).

21. J. Zhou, J. Peatross, M.M. Murnane, H.C. Kapteyn, and I.P Christov, Phys. Rev. Lett. 76, 752 (1996).

22. P. Sprangle and E. Esarey, Phys. Rev. Lett. 67, 2021 (1991); E. Esarey and P. Sprangle, Phys. Rev. A 45, 5872 (1992).

23. E. Esarey, A. Ting, P. Sprangle, D. Umstadter, and X. Liu, IEEE Trans. Plasma Sci. 21, 95 (1993).

24. P. Sprangle and E. Esarey, Phys. Fluids B 4, 2241 (1`992).

25. C. Durfee and H. Milchberg, Phys. Rev. Lett. 71, 2409 (1993).

26. H. Milchberg, C. Durfee, and J. Lynch, J. Opt. Soc. Am. B 12, 731 (1995); H.M. Milchberg, T.R. Clark, C.G. Durfee III, T.M. Antonsen, and P. Mora, Phys. Plasmas 3, 2149 (1996).

27. A. Zigler, Y. Ehrlich, C. Cohen, J. Krall, and P. Sprangle, J. Opt. Soc. Am. B 13, 68 (1996); Y. Ehrlich, C. Chen, A. Zigler, J. Krall, P. Sprangle, and E. Esarey, Phys. Rev. Lett. 77, 4186 (1996).

28. K. Krushelnick, A. Ting, C.I. Moore, H.R. Burris, E. Esarey, P. Sprangle, and M. Baine, submitted to PRL.

29. X. Liu and D. Umstadter, in Short Wavelength V: Physics with Intense Laser Pulses, edited by M.D. Perry and P.B. Corkum (Optical Society of America, Washington, DC, (1993), Vol. 17, pp. 45-49; A. Braun, G. Korn, X. Liu, D. Du, J. Squier, and G. Mourou, Opt. Lett. 20, 73 (1995).

30. P. Sprangle, E. Esarey, and J. Krall, Phys. Rev. E. 54, 4211 (1996).

31. C.E. Max, J. Arons, and A.B. Langdon, Phys. Rev. Lett. 33, 209 (1974).

32. A.L. Berkhoer and V.E. Zakharov, Soviet Phys. JETP, 31, 486 (1970).

33. C.J. McKinstrie and R. Bingham, Phys. Fluids B 4, 2626 (1992).

34. J.F. Drake, P.K. Kaw, Y.C. Lee, G. Schmidt, C.S. Liu, and M.N. Rosenbluth, Phys. Fluids 7, 778 (1974); K. Estabrook and W.L. Kruer, Phys. Fluids 26, 1892 (1983).

35. W.L. Kruer, The Physics of Laser Plasma Interactions, (Addison-Wesley, New York, 1988).

36. T.M. Antonsen, Jr. and P. Mora, Phys. Rev. Lett. 69, 2204 (1992); Phys. Fluids B 5, 1440 (1993).

37. W.B. Mori, C.D. Decker, D.E. Kinkel, and T. Katsouleas, Phys. Rev. Lett. 72, 1482 (1994); C.D. Decker, W.B. Mori, and T. Katsouleas, Phys. Rev. E 50, 3338 (1994).

38. P. Sprangle, J. Krall, E. Esarey, Phys. Rev. Lett. 73, 3544 (1994); E. Esarey, J. Krall, and P. Sprangle, Phys. Rev. Lett. 72, 2887 (1994).

39. A.G. Litvak, Zh. Eksp, Teor. Fiz. 57, 629 (1969) [Sov. Phys. JETP 30, 344 (1969)].

40. P. Sprangle, C.M. Tang, and E. Esarey, IEEE Trans. Plasma Sci. PS-15, 145 (1987).

41. G. Schmidt and W. Horton, Comments Plasma Phys. 9, 85 (1985); G.Z. Sun, E. Ott, Y.C. Lee, and P. Guzdar, Phys. Fluids 30, 526 (1987); A.B. Borisov, A.V. Borovskiy, O.B.

Shiryaev, V.V. Korobkin, A.M. Prokhorov, J.C. Solem, T.S. Luk, K Boyer, and C.K. Rhodes, Phys. Rev. A 45, 5830 (1992).

42. J.F. Reintjes, Nonlinear Optical Parametric Processes in Liquids and Gases (Academic, Orlando, FL, 1984).

43. Y.R. Shen, The Principles of Nonlinear Optics (Wiley, New York, 1984).

44. R.W. Boyd, Nonlinear Optics (Academic, San Diego, 1993).

45. S.E. Harris, Phys. Rev. Lett. 77, 5357 (1996).

46. G.P. Agrawal, Nonlinear Fiber Optics (Academic, San Diego, 1995).

47. L.V. Keldysh, Zh. Eksp. Teor. Fiz. 47, 1945 (1964) [Sov. Phys. JETP 20, 1307 (1965)].

48. L.D. Landau and B.M. Lifshitz, Quantum Mechanics (Pergammon, Oxford, 1977), Sec. 77.

49. M.V. Ammosov, N.B. Delone, and V.P. Krainov, Zh. Eksp. Teor. Fiz. 91, 2008 (1986) [Sov. Phys. JETP 64, 1191 (1987)].

50. S. Augst, D.D. Meyerfoher, D. Strickland, and S.L. Chin, J. Opt. Soc. Am. B 8, 858 (1991).

51. C. Grey-Morgan, Rep. Prog. Phys. 38, 621 (1975).

52. L.J. Radziemski and D.A. Cremers, Laser-Induced Plasmas and Applications (Marcel Dekker, Inc., New York, 1989).

53. NRL Plasma Formulary, edited by J.D. Huba, Naval Research Laboratory Publication NRL/PU/6790-94-265 (U.S. GPO, Washington, D.C., 1994).

54. Ya. B. Zeldovich and Yu.P. Raizer Physics of Shock Waves and High-Temperature Hydrodynamic Phenomena (Academic, New York, 1966), Chap. VI.

55. Yu.P. Raizer, Gas Discharge Physics (Wiley, New York, 1994), Chap. 2.

56. M.A. Lieberman and A.J. Lichtenberg, Principles of Plasma Discharges and Material Processing (Wiley, New York, 1994), Chap. 3.

57. S.C. Brown, Basic Data of Plasma Physics (MIT Press, Boston, 1996).

58. J. Dutton, J. Phys. Chem. 4, 577 (1975).

59. J.D. Jackson, Classical Electrodynamics (Wiley, New York, 1975).

60. S. Humphries, Jr., Charged Particle Beams (Wiley, New York, 1990), Chap. 10.

Gas	$\chi^{(3)}$[esu] x 10^{18}	η_2[cm^2/W] x 10^{20}	P_a[GW]	$R=P_p/P_a$
Helium	0.11	0.43	93	31
Neon	0.21	0.80	50	58
Argon	3.4	13	3.1	940
Krypton	8.5	34	1.2	2500
Xenon	27.0	110	0.36	7900
H_2	2.2	8.5	4.7	610
CO_2	4.2	17	2.3	1200
N_2	2.9	11	3.6	790

Table I. Nonlinear index and focusing power for various neutral gases at STP ($n_a = 2.7 \times 10^{19}\ cm^{-3}$) and for linearly polarized $\lambda_0 = 0.5\ \mu m$ light. The relativistic plasma focusing power $P_p[GW] = 17.4\ (\omega_0/\omega_p)^2 = 2.9 \times 10^3$ for $n_p = n_a = 2.7 \times 10^{19}\ cm^{-3}$.

Atom, Molecule	U_I[eV]	σ_m[cm^2] x 10^{16}	α_0
H_2	15.4	1.1	4.5
N	14.6	2.1	7
N_2	15.8	3.1	7
Ar	15.6	3.7	6

Table II. Parameters for modeling the collisional ionization cross section σ_c, Eq. (B9).

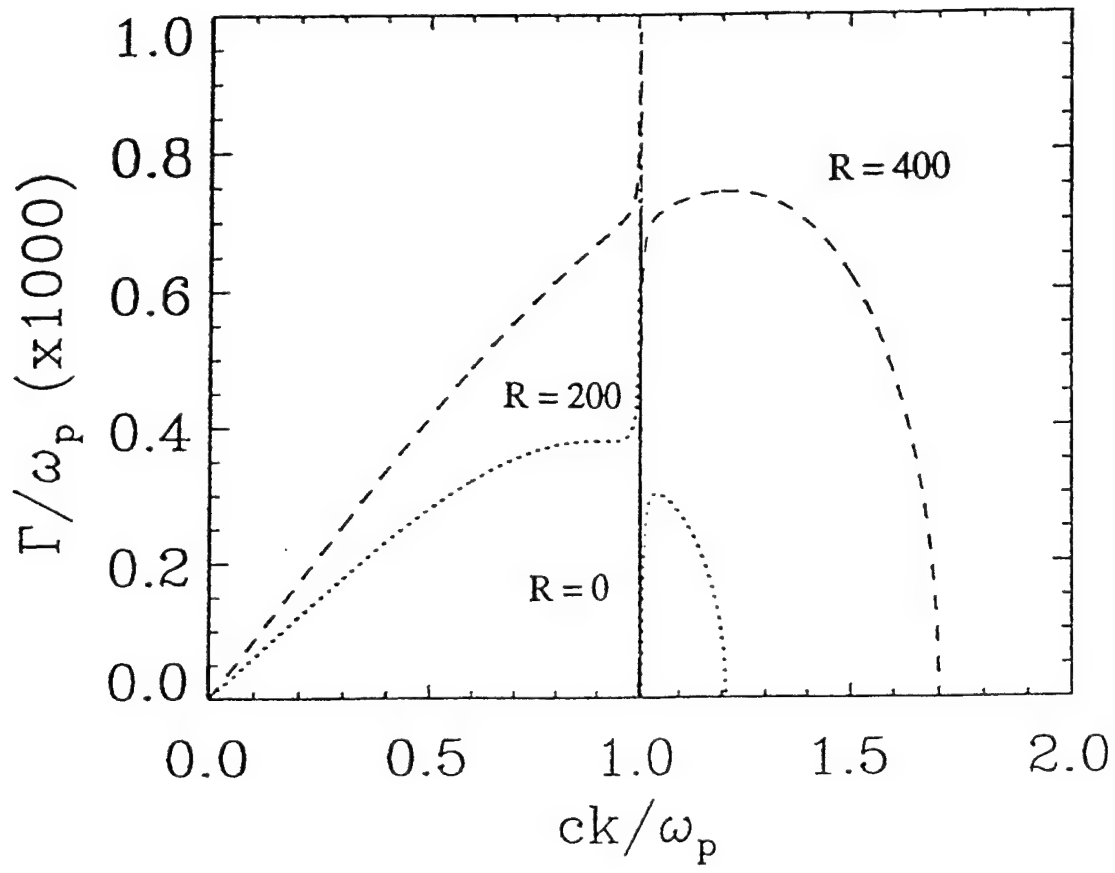

Fig. 1 Normalized modulation and Raman instability growth rate, Γ/ω_p, versus normalized longitudinal wavenumber, ck/ω_p, for $\omega_0/\omega_p = 10$, $a_0 = 0.01$ and (a) R = 0 (solid), (b) R = 200 (dotted), and (c) R = 400 (dashed), where $k_\perp = 0$.

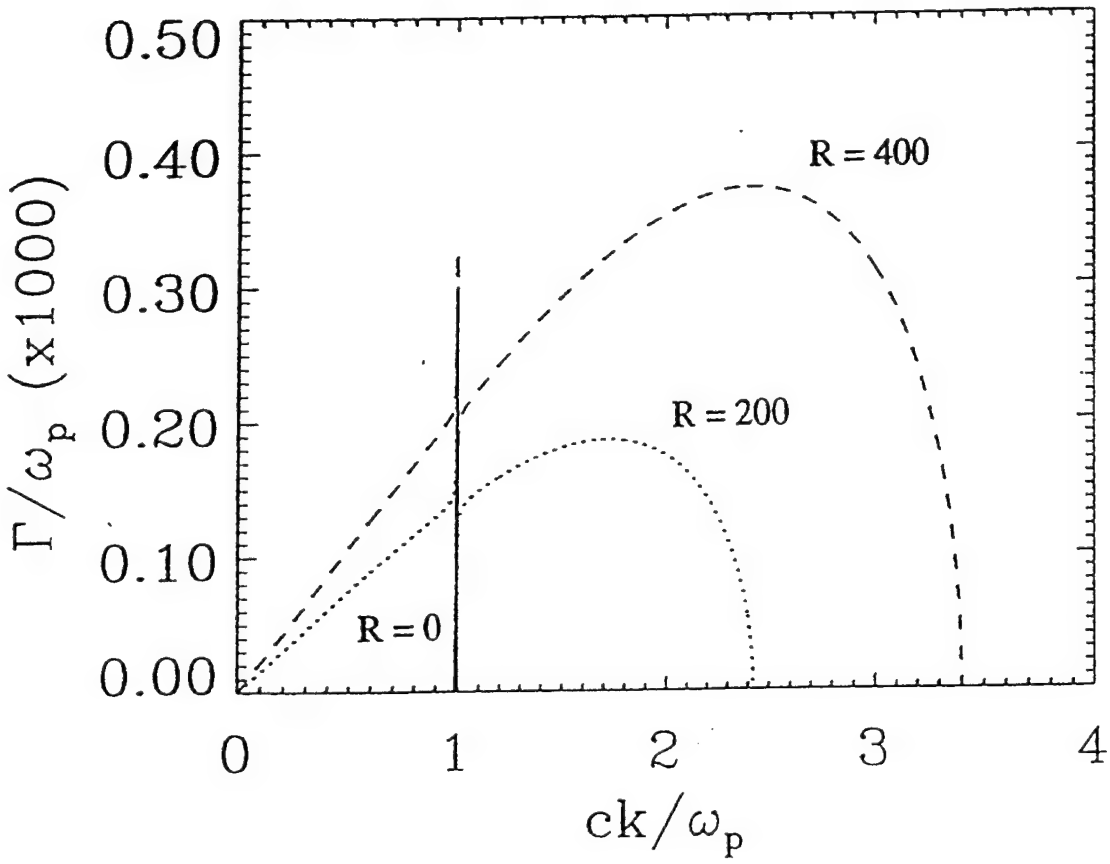

Fig. 2 Normalized modulation and Raman instability growth rate, Γ/ω_p, versus normalized longitudinal wavenumber, ck/ω_p, for $\omega_0/\omega_p = 20$, $a_0 = 0.01$ and (a) R = 0(solid), (b) R = 200 (dotted), and (c) R = 400 (dashed), where $k_\perp = 0$.

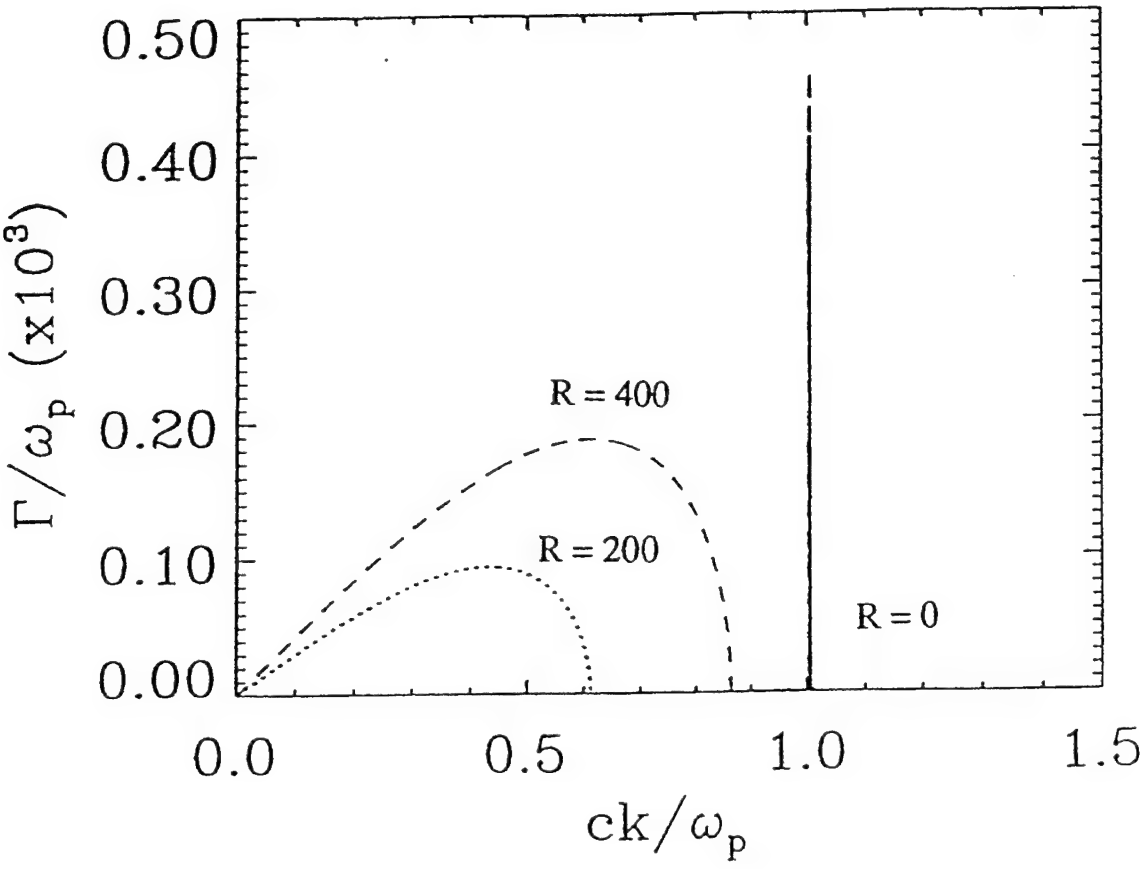

Fig. 3 Normalized modulation and Raman instability growth rate, Γ/ω_p, versus normalized longitudinal wavenumber, ck/ω_p, for $\omega_0/\omega_p = 10$, $a_0 = 0.005$ and (a) R = 0 (solid), (b) R = 200 (dotted), and (c) R = 400 (dashed), where $k_\perp = 0$.

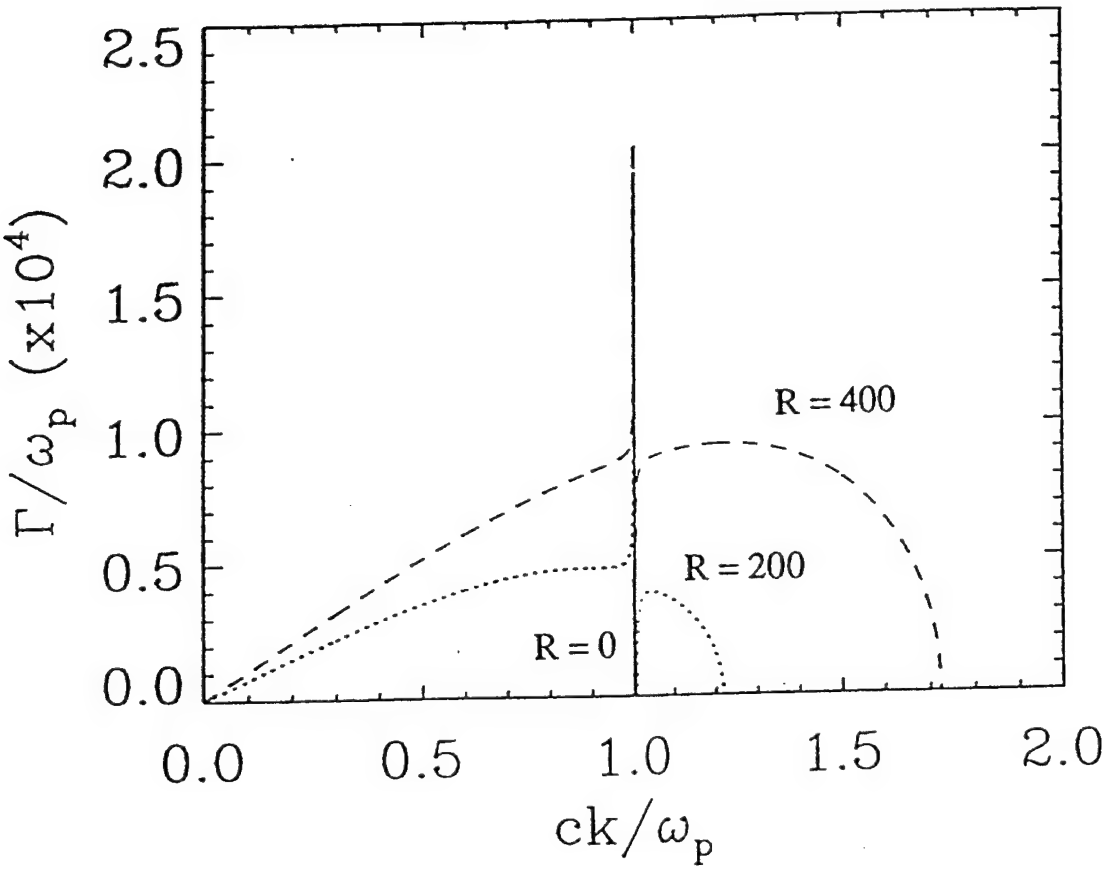

Fig. 4 Normalized modulation and Raman instability growth rate, Γ/ω_p, versus normalized longitudinal wavenumber, ck/ω_p, for $\omega_0/\omega_p = 20$, $a_0 = 0.005$ and (a) R = 0 (solid), (b) R = 200 (dotted), and (c) R = 400 (dashed), where $k_\perp = 0$.

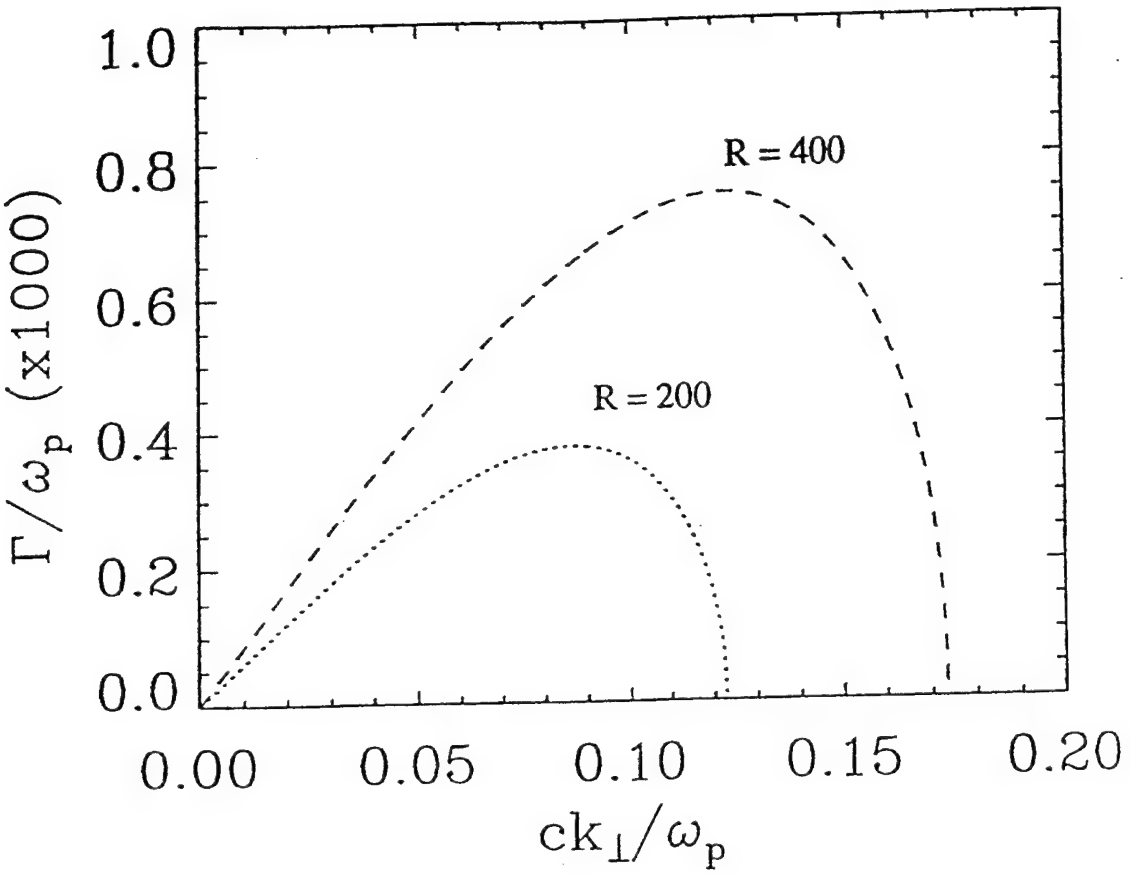

Fig. 5 Normalized filamentation instability growth rate, Γ/ω_p, versus normalized transverse wavenumber, $ck_\perp/\omega_p$, for $\omega_0/\omega_p = 10$, $a_0 = 0.01$ and (a) R = 200 (dotted), and (b) R = 400 (dashed), where k = 0.

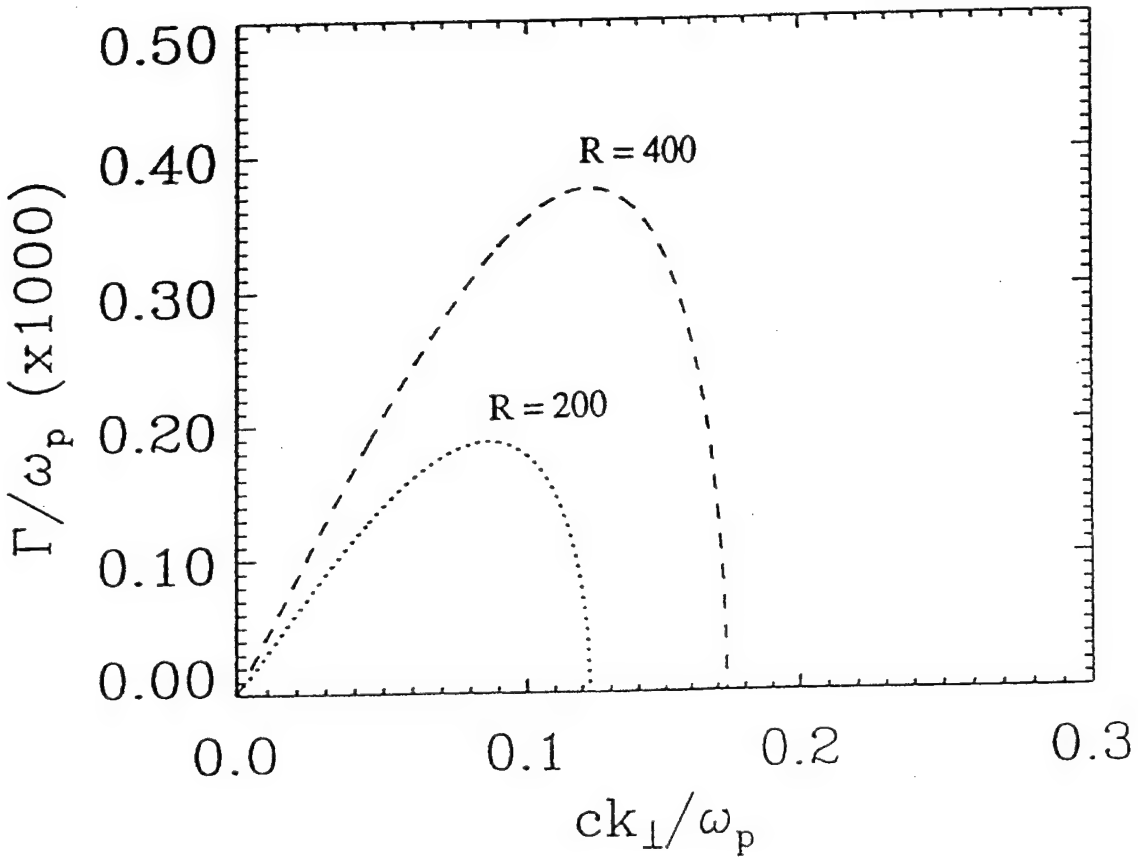

Fig. 6 Normalized filamentation instability growth rate, Γ/ω_p, versus normalized transverse wavenumber, $ck_\perp/\omega_p$, for $\omega_0/\omega_p = 20$, $a_0 = 0.01$ and (a) R = 200 (dotted), and (b) R = 400 (dashed), where k = 0.

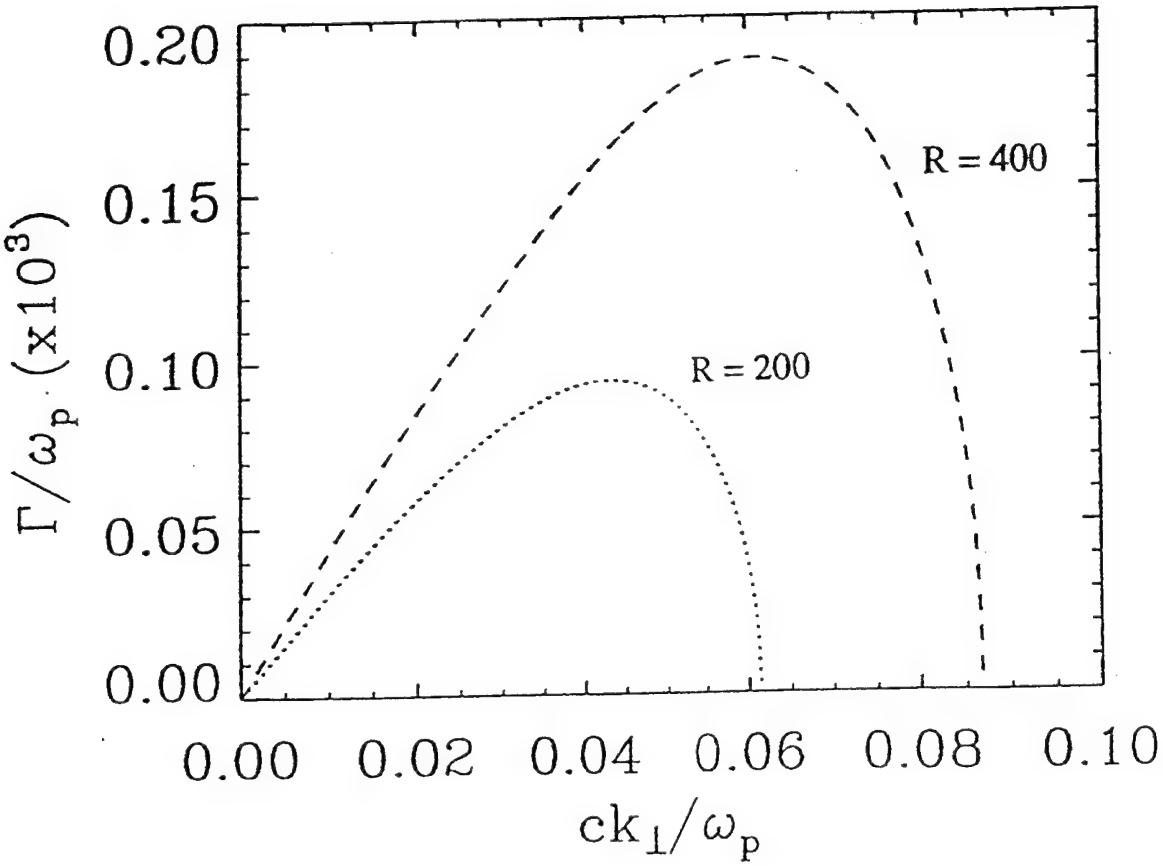

Fig. 7 Normalized filamentation instability growth rate, Γ/ω_p, versus normalized transverse wavenumber, $ck_\perp/\omega_p$, for $\omega_0/\omega_p = 10$, $a_0 = 0.005$ and (a) R = 200 (dotted), and (b) R = 400 (dashed), where k = 0.

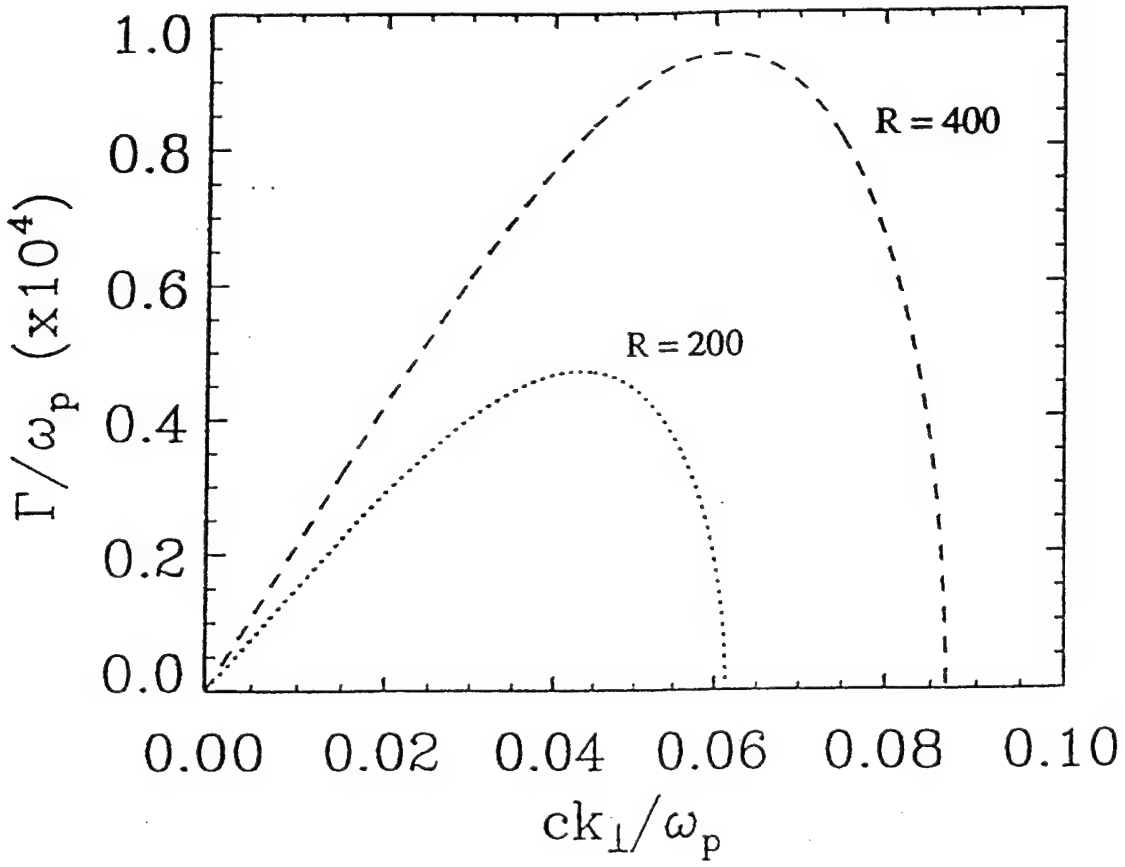

Fig. 8 Normalized filamentation instability growth rate, Γ/ω_p, versus normalized transverse wavenumber, $ck_\perp/\omega_p$, for $\omega_0/\omega_p = 20$, $a_0 = 0.005$ and (a) R = 200 (dotted), and (b) R = 400 (dashed), where k = 0.

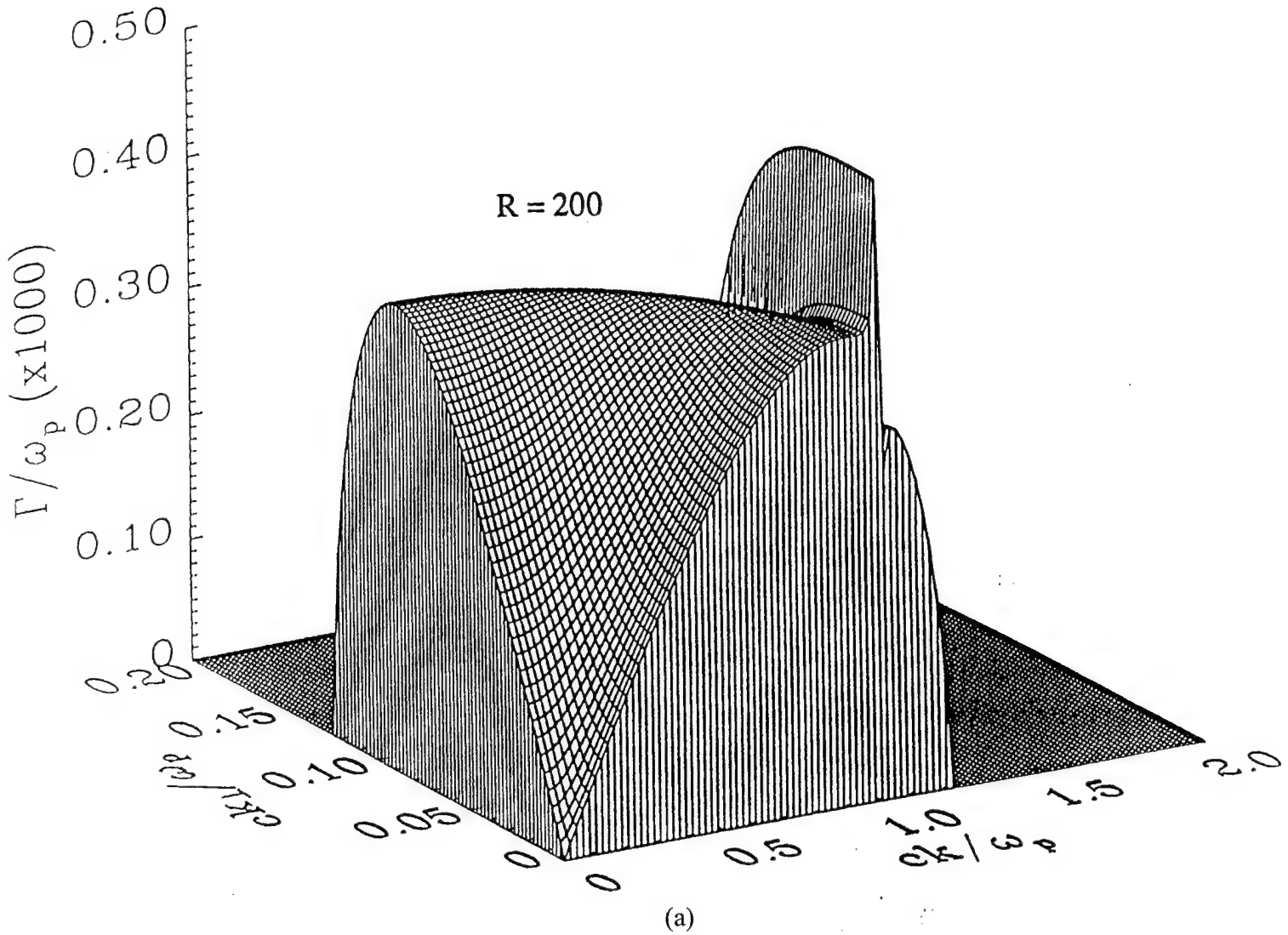

(a)

Fig. 9 Surface plots of normalized growth rate as a function of ck/ω_p and $ck_\perp/\omega_p$, for (a) R = 200 and (b) R = 400, where $a_0 = 0.01$ and $\omega_0/\omega_p = 10$.

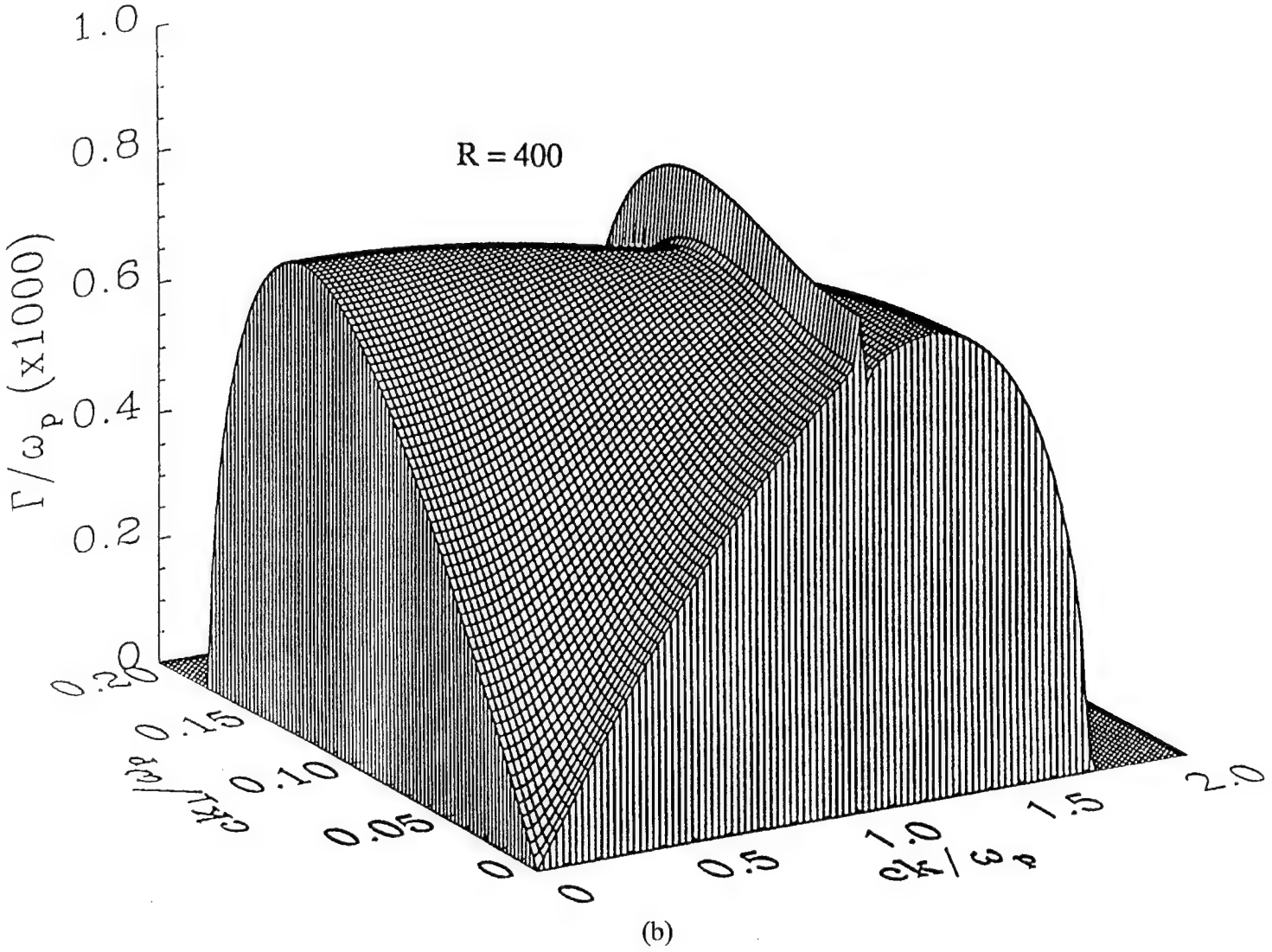

(b)

Fig. 9 (Continued) Surface plots of normalized growth rate as a function of ck/ω_p and $ck_\perp/\omega_p$, for (a) R = 200 and (b) R = 400, where $a_0 = 0.01$ and $\omega_0/\omega_p = 10$.

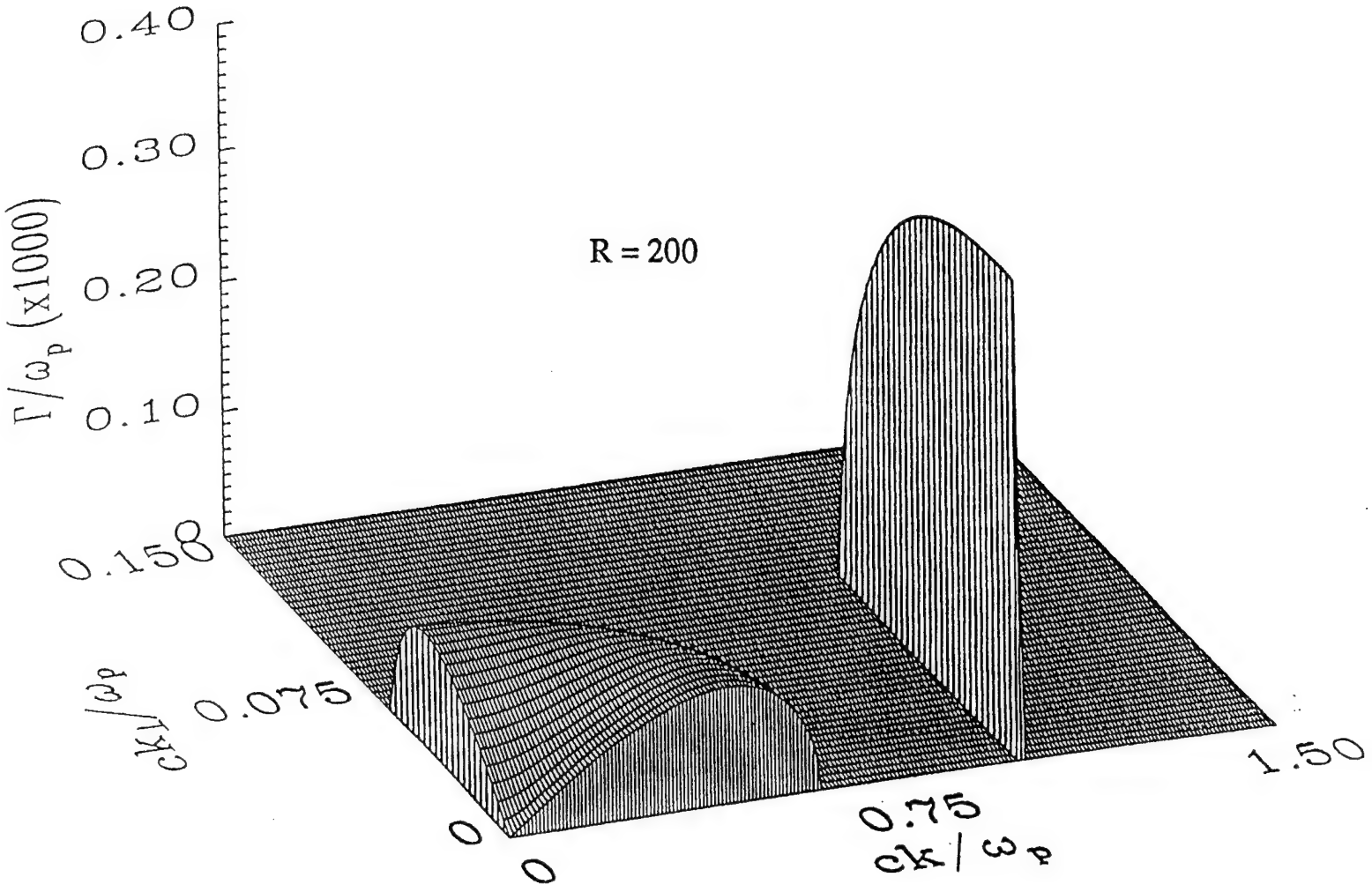

(a)

Fig. 10 Surface plots of normalized growth rate as a function of ck/ω_p and $ck_\perp/\omega_p$, for (a) R = 200 and (b) R = 400, where $a_0 = 0.005$ and $\omega_0/\omega_p = 10$.

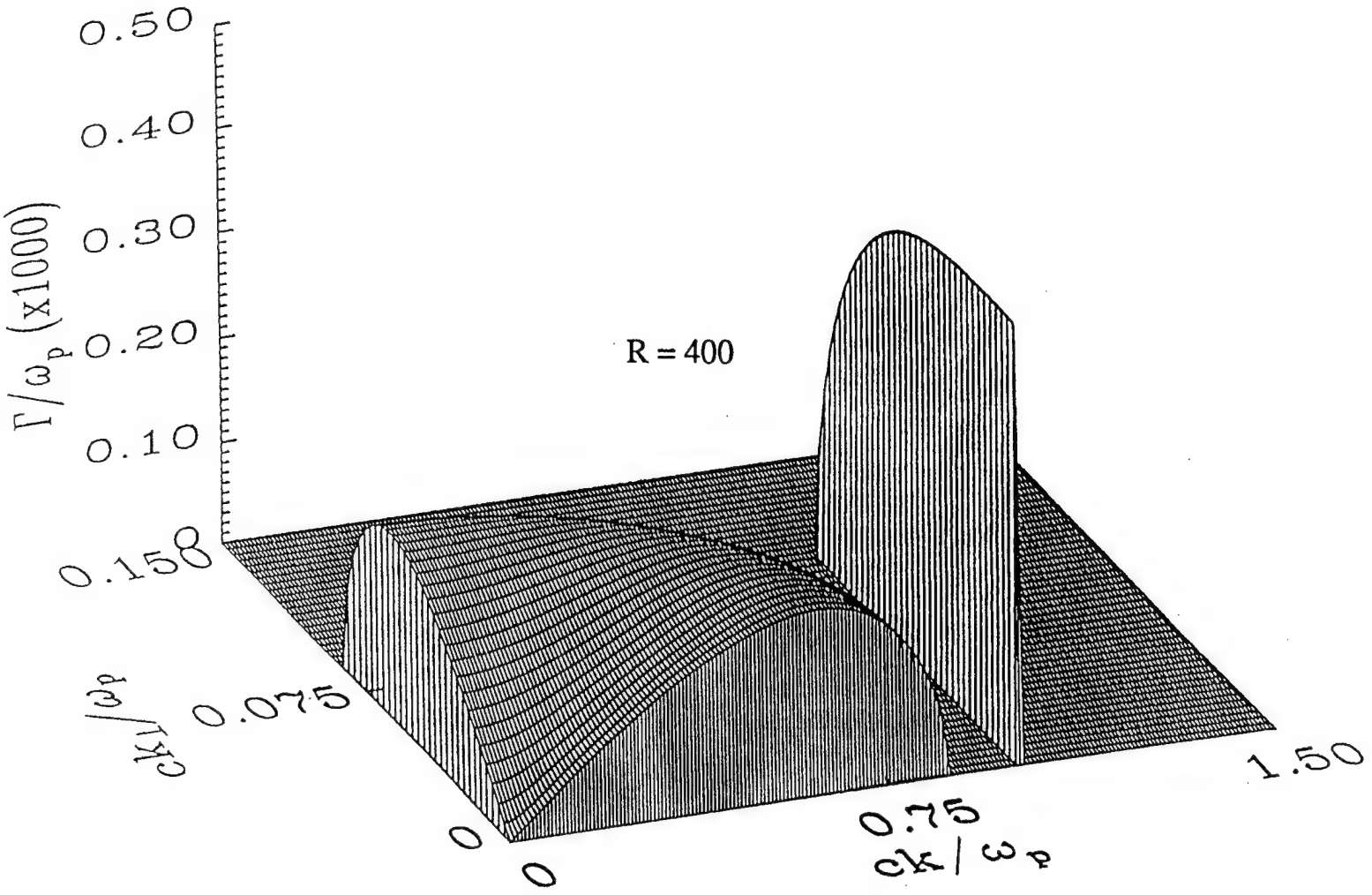

(b)

Fig. 10 (Continued) Surface plots of normalized growth rate as a function of ck/ω_p and $ck_\perp/\omega_p$, for (a) R = 200 and (b) R = 400, where $a_0 = 0.005$ and $\omega_0/\omega_p = 10$.

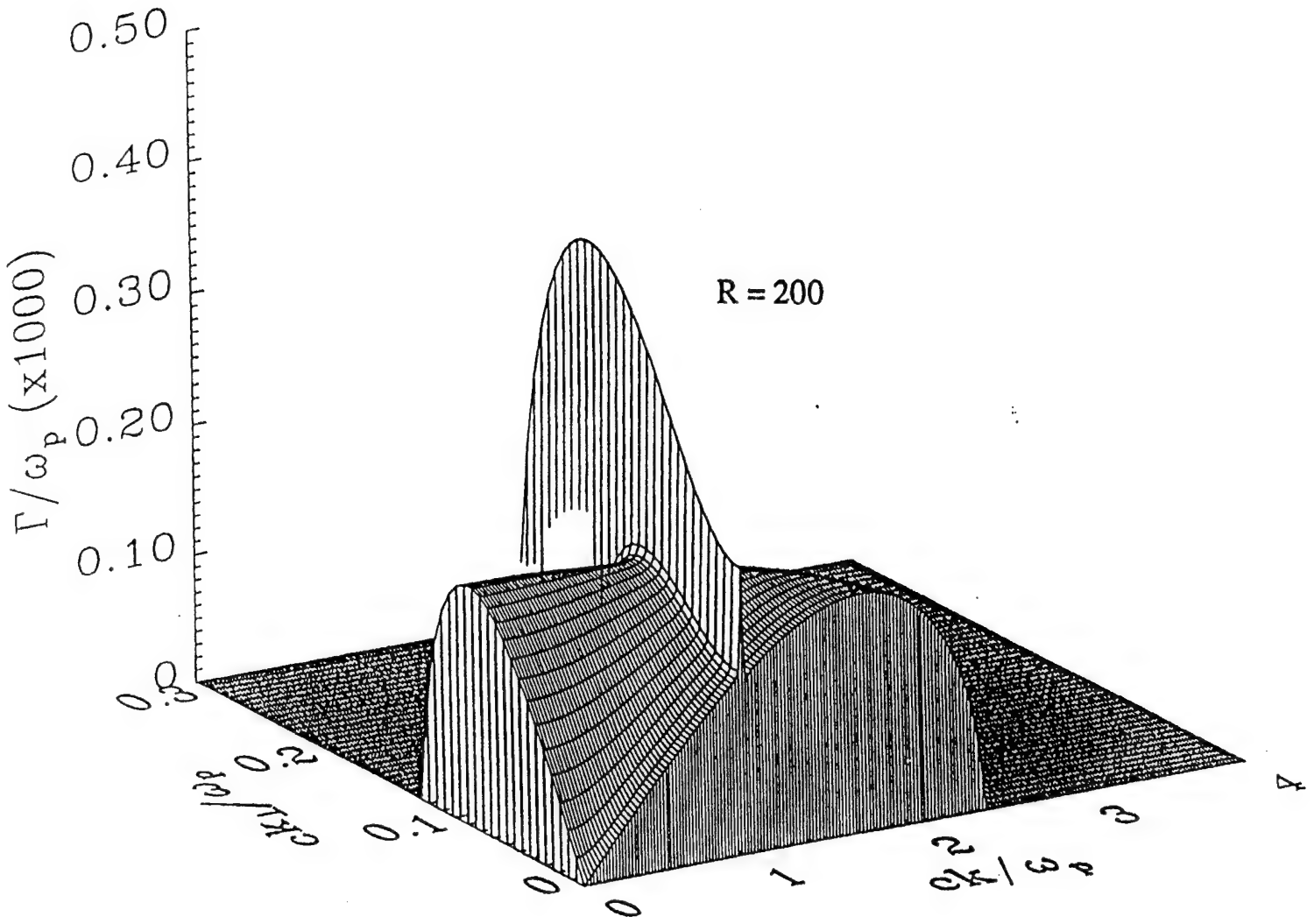

(a)

Fig. 11 Surface plots of normalized growth rate as a function of ck/ω_p and $ck_\perp/\omega_p$, for (a) R = 200 and (b) R = 400, where $a_0 = 0.01$ and $\omega_0/\omega_p = 20$.

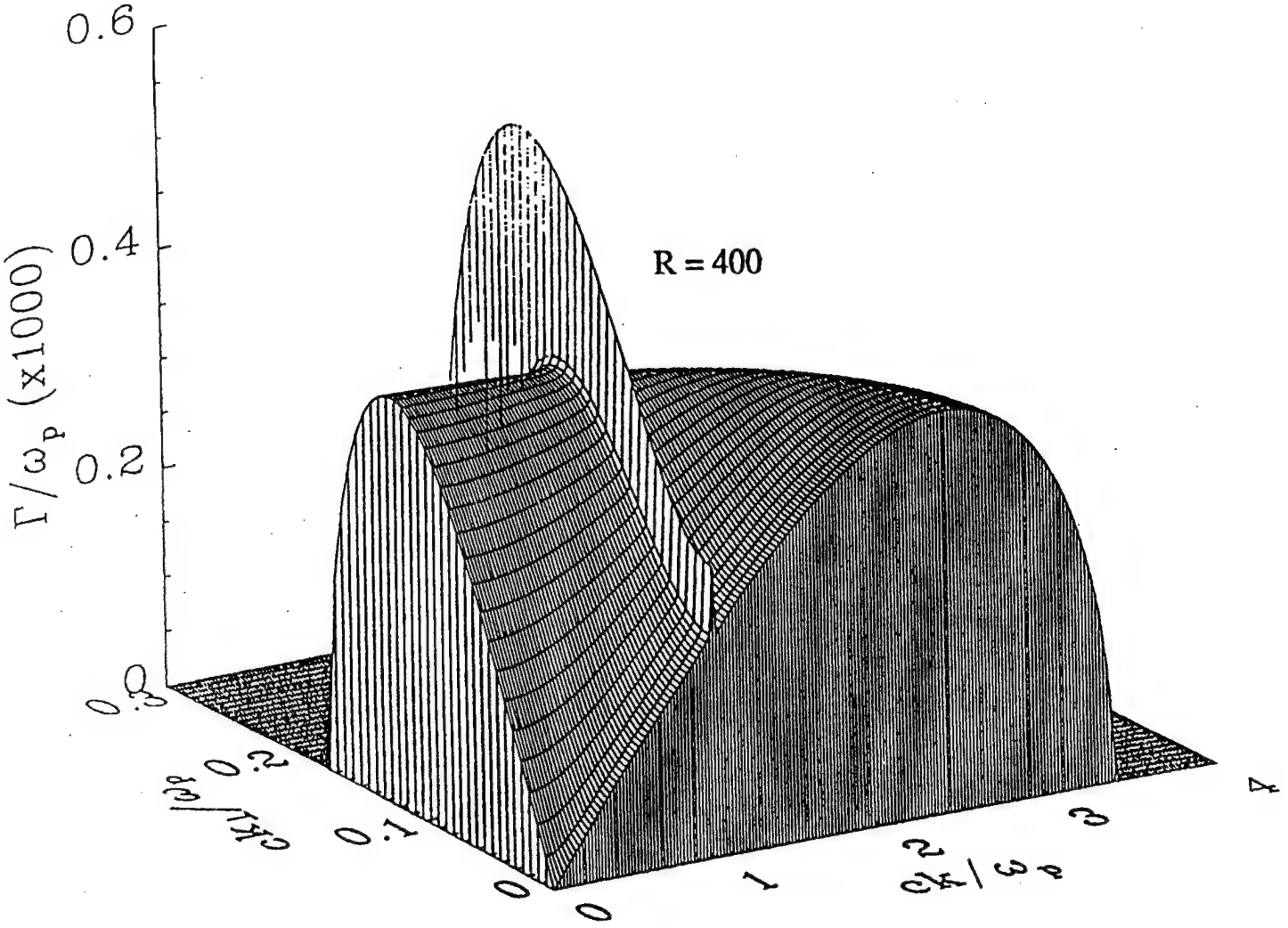

(b)

Fig. 11 (Continued) Surface plots of normalized growth rate as a function of ck/ω_p and $ck_\perp/\omega_p$, for (a) R = 200 and (b) R = 400, where $a_0 = 0.01$ and $\omega_0/\omega_p = 20$.

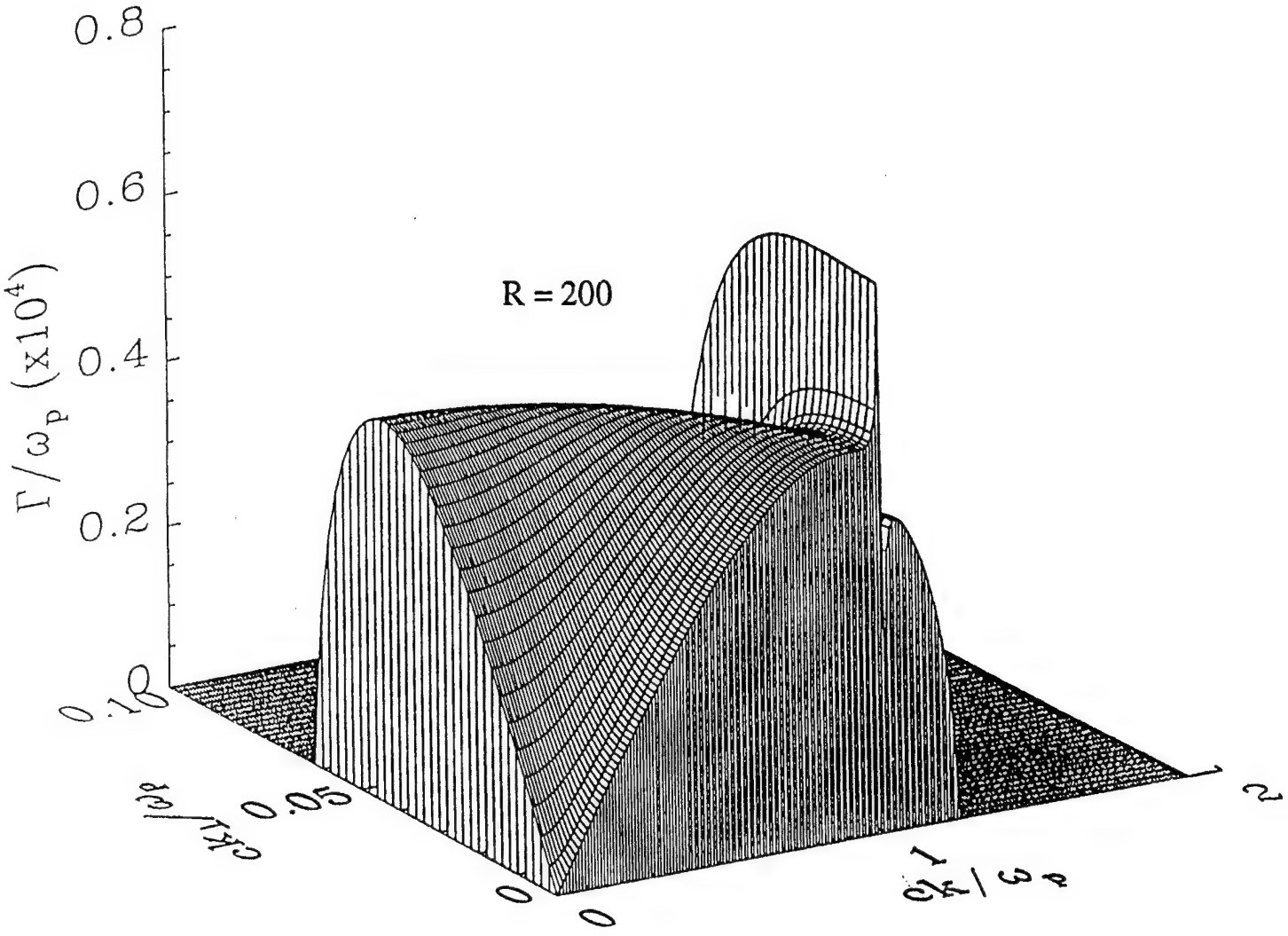

(a)

Fig. 12 Surface plots of normalized growth rate as a function of ck/ω_p and $ck_\perp/\omega_p$, for (a) R = 200 and (b) R = 400, where $a_0 = 0.005$ and $\omega_0/\omega_p = 20$.

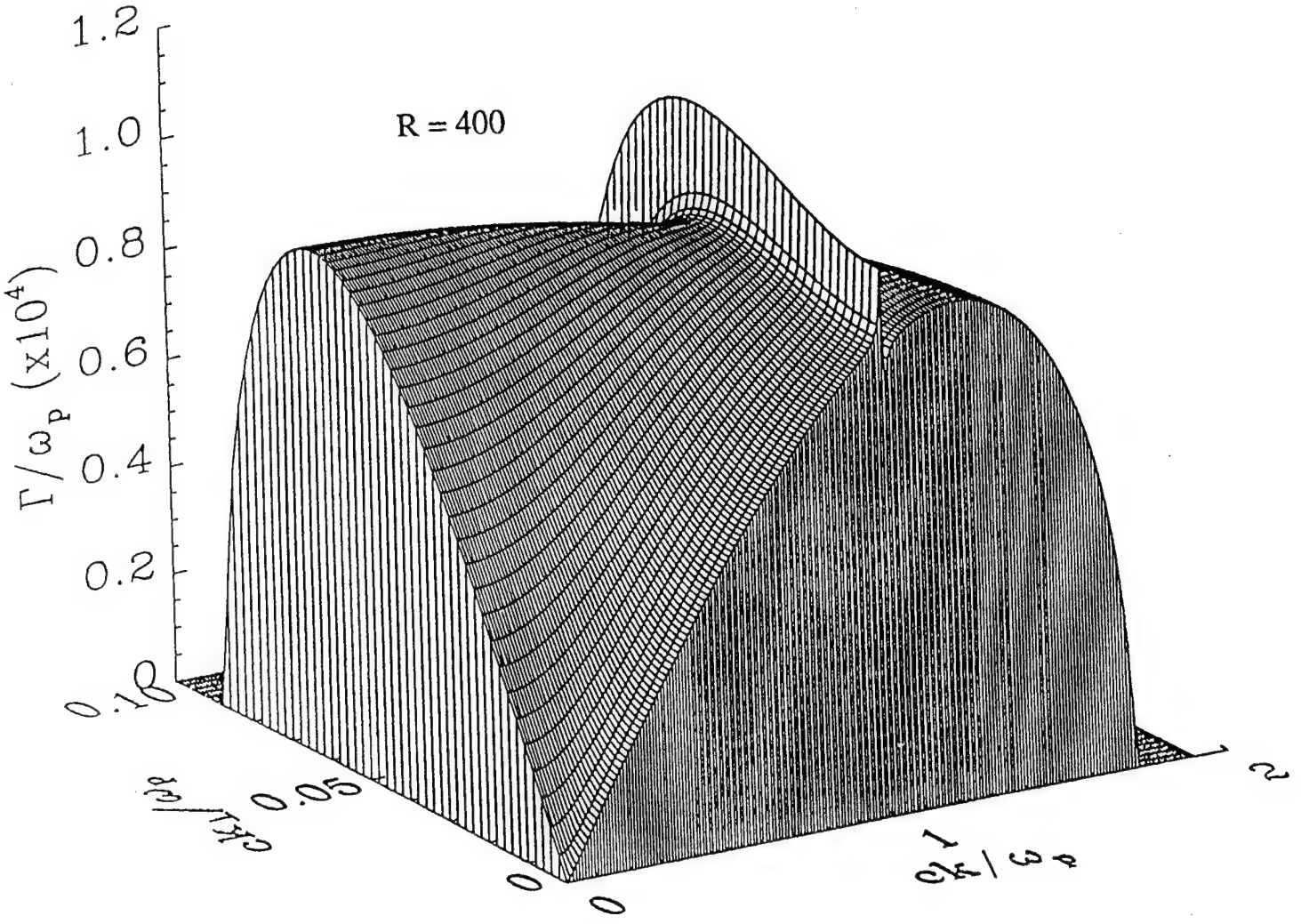

(b)

Fig. 12 (Continued) Surface plots of normalized growth rate as a function of ck/ω_p and $ck_\perp/\omega_p$, for (a) $R = 200$ and (b) $R = 400$, where $a_0 = 0.005$ and $\omega_0/\omega_p = 20$.

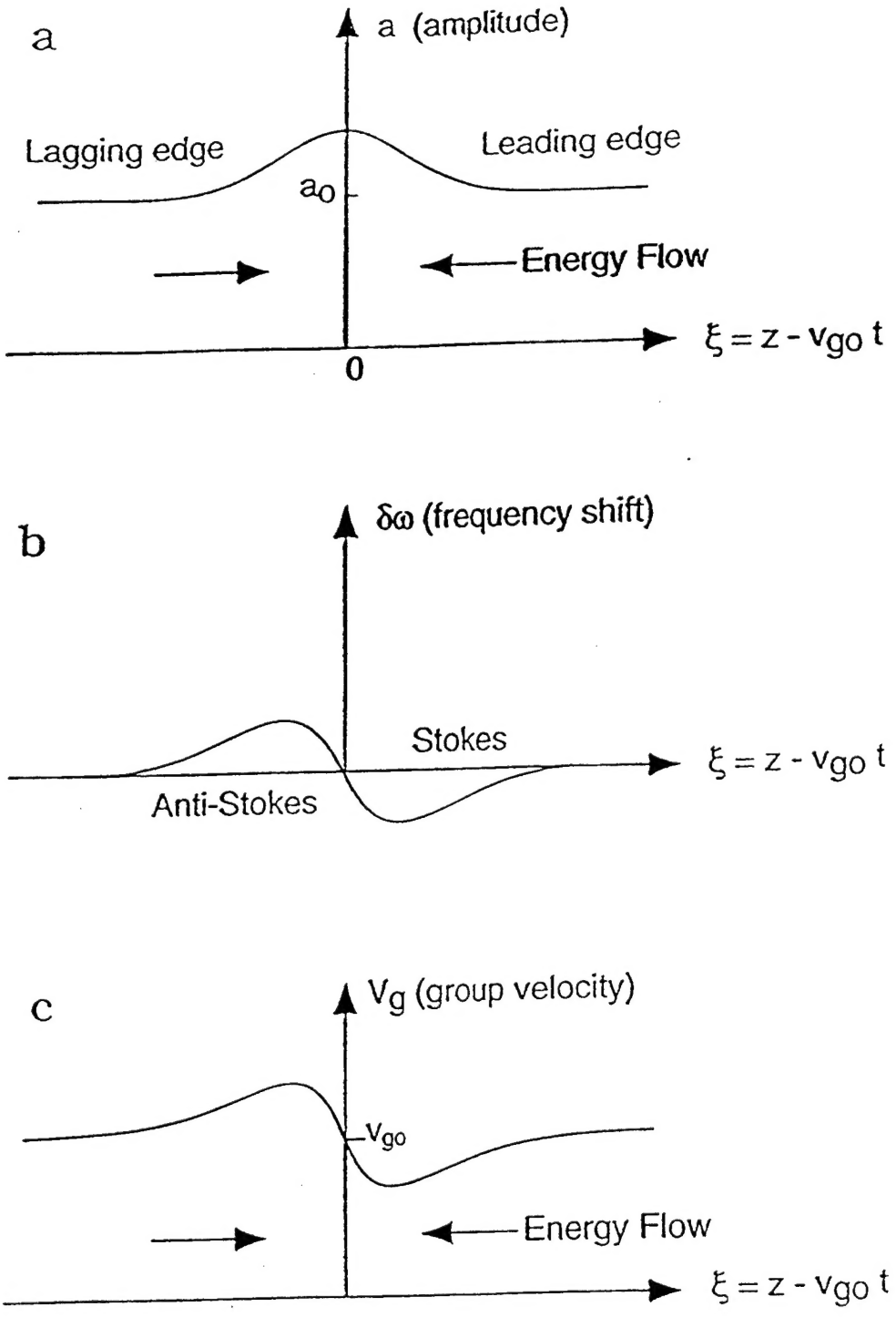

Fig. 13 Illustration of the physical mechanism for the modulation instability in the linear group velocity frame: (a) shows initial perturbation in amplitude, (b) shows frequency shift induced by self-phase modulation and (c) shows group velocity dispersion indicating that energy flows towards the initial perturbation resulting in growth.

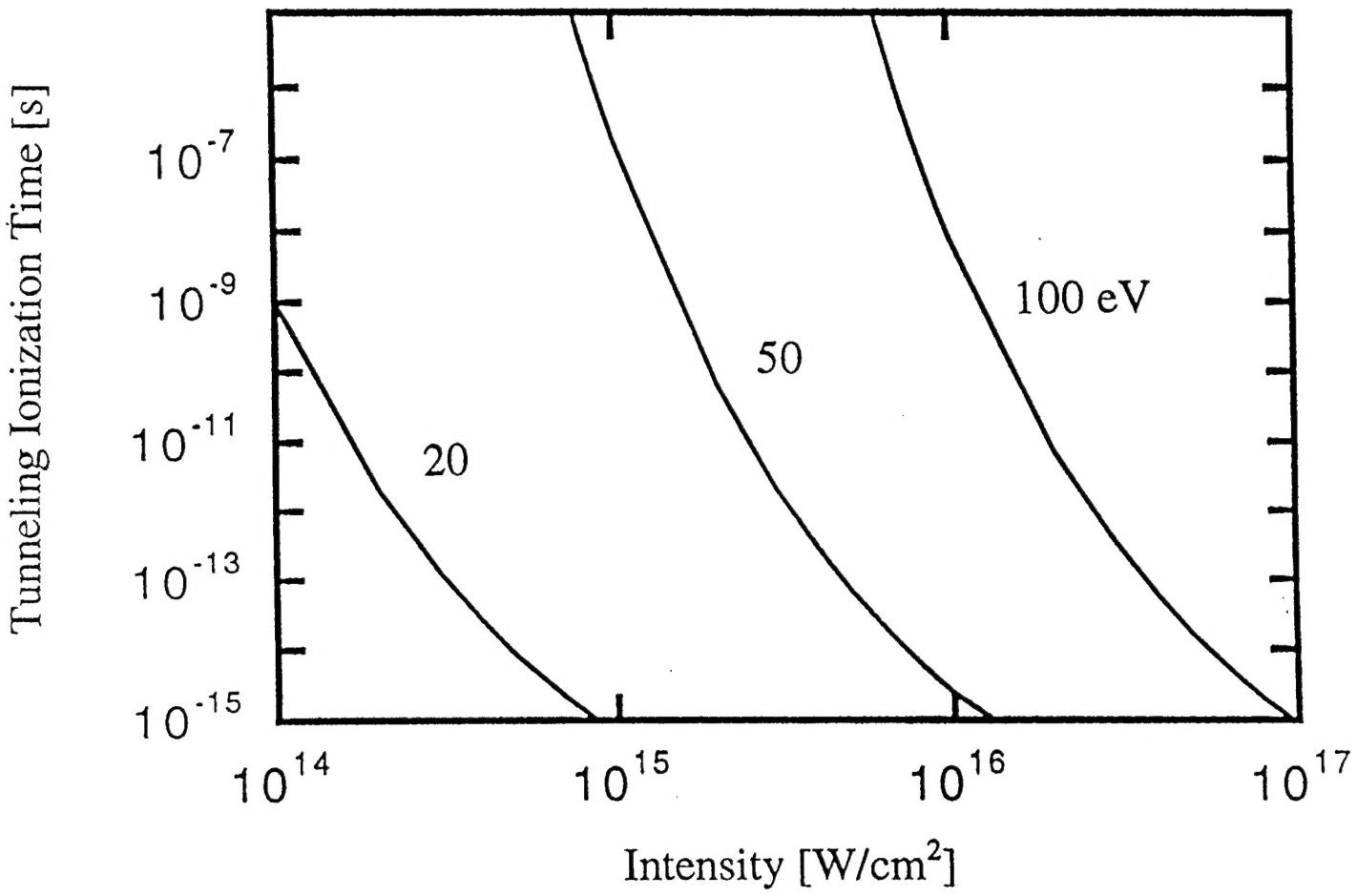

Fig. 14 Tunneling ionization time, $1/W_t$, as a function of laser intensity for various ionization energies, (a) $U_I = 20$ eV, (b) $U_I = 50$ eV and (c) $U_I = 100$ eV.

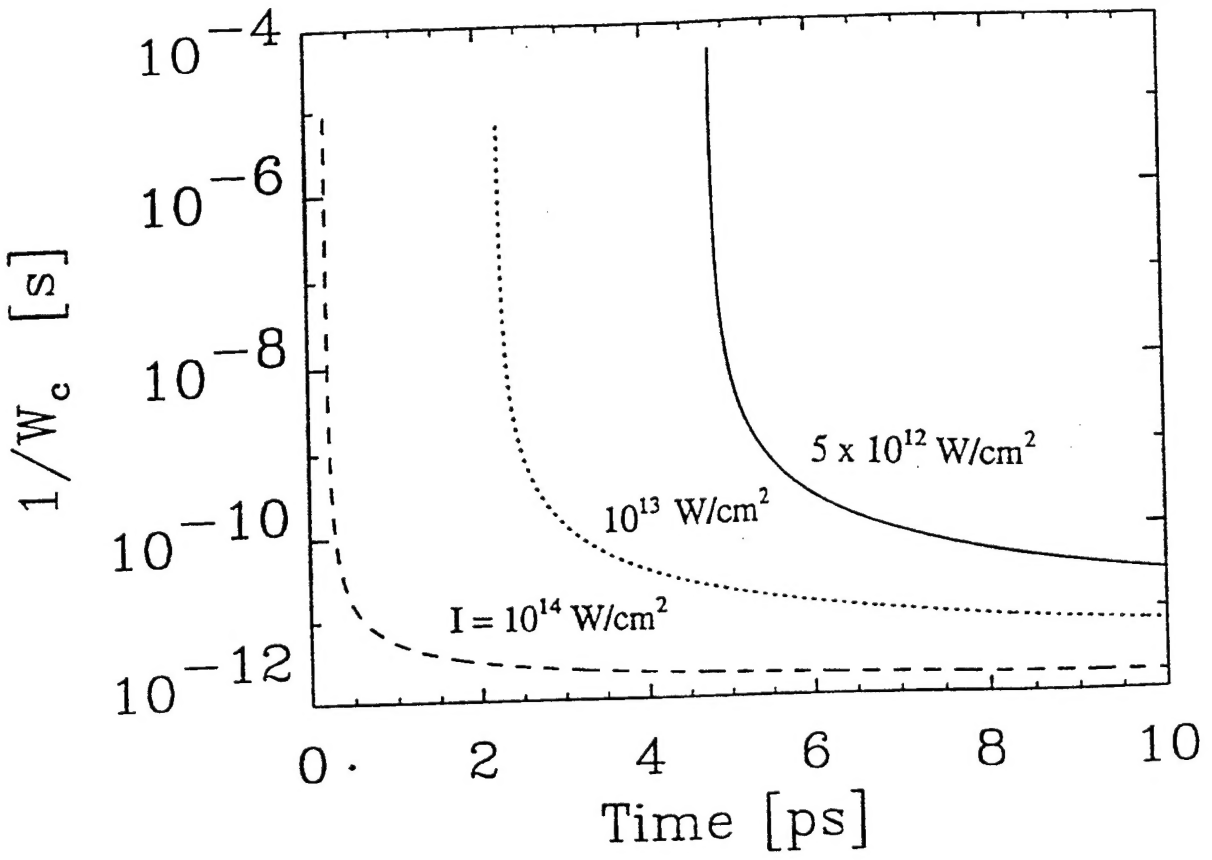

Fig. 15 Collisional ionization time, $1/W_c$, as a function of time in the low energy limit ($U_{0s} << U_I$), Eq. (B11), for various laser intensities, (a) I = 10^{14} W/cm^2 (dashed), (b) I = 10^{13} W/cm^2 (dotted) and (c) I = 5×10^{12} W/cm^2 (solid), where $n_a = 2.7 \times 10^{19}$ cm^{-3}, $\nu_m = 5 \times 10^{12}$ sec^{-1}, $\nu_u = 5 \times 10^{10}$ sec^{-1}, $\sigma_m = 2 \times 10^{-16}$ cm^2, $U_I = 20$ eV, and $\alpha_0 = 5$.

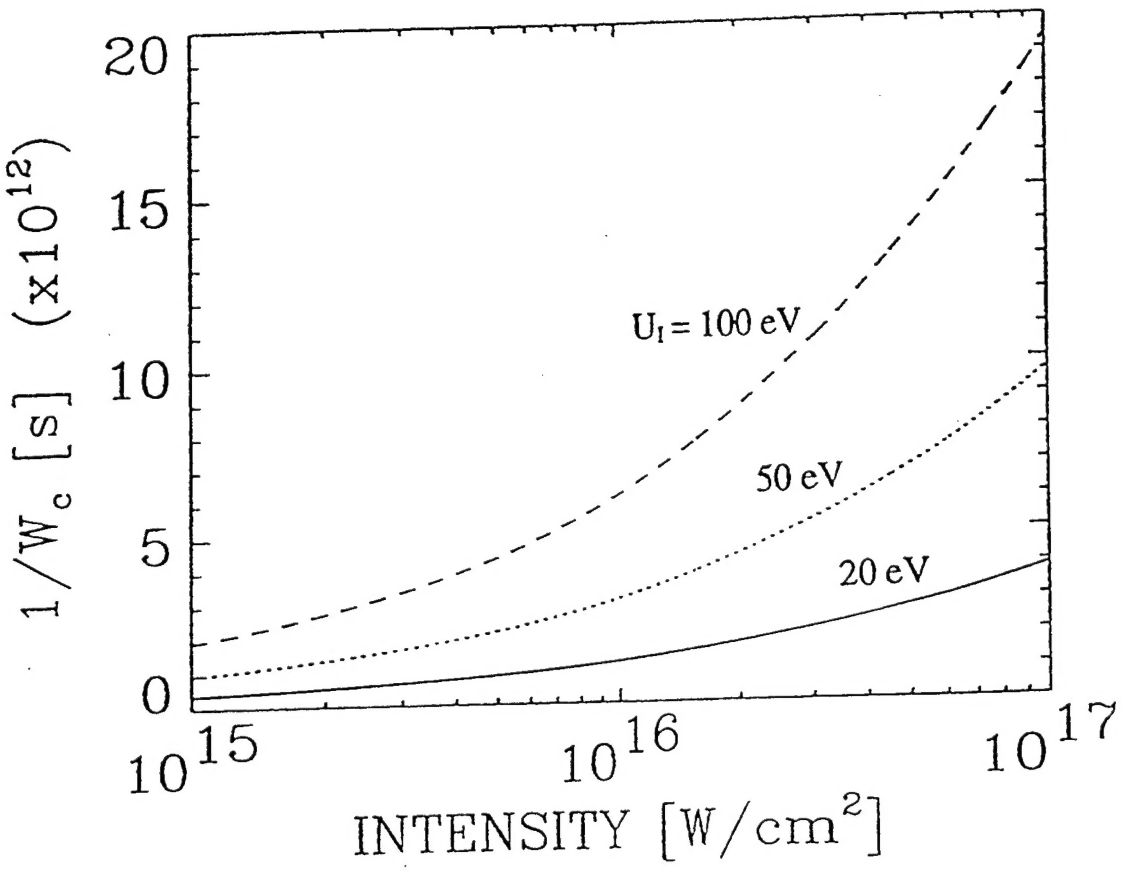

Fig. 16 Collisional ionization time, $1/W_c$, in the high energy limit ($U_{0s} >> U_I$), Eq. (B19), as a function of laser intensity for various ionization energies, (a) U_I = 20 eV (solid), (b) U_I = 50 eV (dotted) and (c) U_I = 100 eV (dashed), where $n_a = 2.7 \times 10^{19}$ cm^{-3}, Z = 1 and $\ell n\Lambda = 10$.